Constraining the magnitude of the global dust cycle by minimizing the difference between a model and observations

R. V. Cakmur,[1,2] R. L. Miller,[2,3] J. Perlwitz,[2,3] I. V. Geogdzhayev,[2,3] P. Ginoux,[4] D. Koch,[2,5] K. E. Kohfeld,[6] I. Tegen,[7] and C. S. Zender[8]

Received 21 January 2005; revised 30 September 2005; accepted 17 November 2005; published 29 March 2006.

[1] Current estimates of global dust emission vary by over a factor of two. Here, we use multiple data types and a worldwide array of stations combined with a dust model to constrain the magnitude of the global dust cycle for particles with radii between 0.1 and 8 μm. An optimal value of global emission is calculated by minimizing the difference between the model dust distribution and observations. The optimal global emission is most sensitive to the prescription of the dust source region. Depending upon the assumed source, the agreement with observations is greatest for global, annual emission ranging from 1500 to 2600 Tg. However, global annual emission between 1000 and 3000 Tg remains in agreement with the observations, given small changes in the method of optimization. Both ranges include values that are substantially larger than calculated by current dust models. In contrast, the optimal fraction of clay particles (whose radii are less than 1 μm) is lower than current model estimates. The optimal solution identified by a combination of data sets is different from that identified by any single data set and is more robust. Uncertainty is introduced into the optimal emission by model biases and the uncertain contribution of other aerosol species to the observations.

Citation: Cakmur, R. V., R. L. Miller, J. Perlwitz, I. V. Geogdzhayev, P. Ginoux, D. Koch, K. E. Kohfeld, I. Tegen, and C. S. Zender (2006), Constraining the magnitude of the global dust cycle by minimizing the difference between a model and observations, *J. Geophys. Res.*, *111*, D06207, doi:10.1029/2005JD005791.

1. Introduction

[2] Aerosols are an important component of the global radiation budget. Mineral (or 'soil') dust aerosols are one of the largest contributors to aerosol radiative forcing [*Tegen et al.*, 1997; *Penner et al.*, 2001]. In order to compute this forcing, accurate information is needed on the distribution of dust within the atmosphere along with the particle size distribution. These properties have uncertainties associated with them and therefore contribute to the uncertainty of dust radiative forcing [*Houghton et al.*, 2001]. This study concentrates on constraining the geographic and particle size distribution of dust aerosols.

[3] Dust emission, whereby soil particles enter the atmosphere, has been measured at only a small number of locations over a relatively short period of time [*Tegen et al.*, 2002]. A global value has been extrapolated from limited observations over specific source regions, such as the Sahara and Asia [*Uematsu et al.*, 1985; *Swap et al.*, 1996; *Marticorena and Bergametti*, 1996; *Zhang et al.*, 1997]. The global sum resulting from these measurements ranges over two orders of magnitude from 60 to 5,000 Tg/yr [*Schutz*, 1980; *Goudie*, 1983; *Duce*, 1995; *Goudie and Middleton*, 2001]. Oceanic deposition observations represent a potential lower bound on global emission but are scarce.

[4] Dust emission is estimated indirectly by constraining a model with observations of aerosol amount. Modelers are confronted with difficulties because dust emission is a nonlinear function of wind speed that depends on many other factors that are poorly known on the scale of the model grid. Emission $\mathcal{E}$ is often calculated according to:

$$\mathcal{E} = \begin{cases} CF(r)(w - w_t)w^2 & \text{for } w \geq w_t \\ 0 & \text{for } w < w_t \end{cases} \quad (1)$$

where w is the surface wind speed, w_t is the threshold above which emission occurs, C is a coefficient of proportionality,

[1]National Academy of Sciences, Washington, D. C., USA.
[2]NASA Goddard Institute for Space Studies, New York, New York, USA.
[3]Department of Applied Physics and Applied Math, Columbia University, New York, New York, USA.
[4]Geophysical Fluid Dynamics Laboratory, NOAA, Princeton, New Jersey, USA.
[5]Center for Climate Systems Research, Columbia University, New York, New York, USA.
[6]School of Earth and Environmental Sciences, Queens College, City University of New York, Flushing, New York, USA.
[7]Leibniz Institute for Tropospheric Research, Leipzig, Germany.
[8]Department of Earth System Science, University of California, Irvine, California, USA.

Copyright 2006 by the American Geophysical Union.
0148-0227/06/2005JD005791

and $F(r)$ represents the dependence of emission upon particle size, denoted by radius r [*Gillette*, 1974]. The emitted size distribution $F(r)$ depends upon both the size distribution of particles in the soil and the intricate transfer of momentum from the largest particles displaced by the wind to the smallest particles that are buoyant enough to enter the atmosphere [*Alfaro and Gomes*, 2001]. While the coefficient C and size distribution $F(r)$ can be specified empirically in certain situations, neither is well-known on the scale of global models. These parameters are often chosen so that the model dust distribution matches the observations at a particular location such as Barbados, where there are long term measurements [*Prospero*, 1996]. Global emission from recent models varies by over a factor of two between 800 and 2,000 Tg/yr for particle diameters below 10 μm [*Ginoux et al.*, 2001; *Tegen et al.*, 2002; *Mahowald et al.*, 2002; *Zender et al.*, 2004]. Global emission is sensitive to the data set and region used as a model constraint, in addition to the physics of the model.

[5] In this article, we constrain the emission and global distribution of dust aerosols using multiple data types and a worldwide array of stations. Using the dust distribution calculated by the NASA Goddard Institute for Space Studies (GISS) atmospheric general circulation model (AGCM), we minimize the squared difference between the model distribution and observations to derive an optimal value of global dust emission. More precisely, we vary clay and silt emission separately through the product $CF(r)$ in order to identify values that are in best agreement with observations. (Clay particles are defined with radius r less than 1 μm, compared to larger silt particles.)

[6] In section 2, we review the parameterization of dust aerosols within the GISS AGCM [*Miller et al.*, 2006]. We describe the data types used to constrain the model in section 3. In section 4, we discuss the minimization procedure used to derive a dust cycle that is in optimal agreement with observations. In section 5, we calculate the optimal global emission of clay and silt particles, along with a range of emission that agrees nearly as well with the observations. We also calculate the sensitivity of the optimal value to different data sets and how this value changes if we constrain the model for specific regions such as Africa, Asia, and Barbados. Our conclusions are given in section 6.

2. Dust Model

[7] Dust aerosol is calculated using the newly available modelE AGCM of the NASA Goddard Institute for Space Studies [*Schmidt et al.*, 2006]. The dust model represents a substantial upgrade to the version developed by *Tegen and Miller* [1998], and is described in more detail in a companion article [*Miller et al.*, 2006].

[8] The AGCM has horizontal resolution of 4° latitude by 5° longitude and 20 layers extending from the surface to 0.1 mb, of which 10 are in the troposphere. The planetary boundary layer (PBL) is simulated using a non-local, second-order model of turbulence that extends throughout the depth of the atmosphere [*Cheng et al.*, 2002], an improvement to the previous version of the GISS model where turbulent mixing occurred only up to the middle of the first layer around 200 m. Tracers (including dust) are advected using the quadratic upstream scheme [*Prather*, 1986], which computes the slope and curvature of a tracer in addition to its grid box average, increasing the effective resolution.

[9] The model transports four size categories of soil dust: one for clay with particle radii less than 1 μm, and three for silt with radii of 1–2, 2–4, and 4–8 μm. Particles with radii less than 1 μm are transported as one class because they are not fractionated by gravitational settling, due to the particles' similar fall speeds [*Tegen and Lacis*, 1996]. However, in the radiative transfer calculations, the clay category is further divided into four size bins.

[10] Enclosed basins containing former lake beds or riverine sediment deposits provide an abundance of small clay-sized particles that are loosely bound, and dominate global dust emission according to the Total Ozone Mapping Spectrometer (TOMS) aerosol index satellite retrieval [*Prospero et al.*, 2002]. Modeling studies show that inclusion of these 'preferred' source regions improve the realism of the model dust load in the vicinity of the sources [*Zender et al.*, 2003]. To identify these regions, we choose from several alternative representations based upon topography [*Ginoux et al.*, 2001] (hereafter referred to as GINOUX), the presence of dry lake basins [*Tegen et al.*, 2002] (hereafter TEGEN), an alternative identification of dry lakes (referred to as Geomorphology by *Zender et al.* [2003]) (here referred to as ZENDER1), and a linear function of surface reflectance retrieved from Moderate Resolution Imaging Spectroradiometer (MODIS) [*Grini et al.*, 2005] (hereafter ZENDER2). For the TEGEN case, emission results from a combination of preferred sources and sources identified using conventional vegetation and soil wetness criteria. We weight these so that preferred sources contribute roughly 90% of the global emission, consistent with *Tegen et al.* [2002], although our results are insensitive for fractions as low as 50%. We will consider the sensitivity of our results to the preferred source formulation.

[11] Dust emission depends upon the fraction of the wind stress absorbed by soil particles, as opposed to 'roughness elements' like vegetation and topography; wind erosion of soil decreases with the roughness of the surface. We use the European Remote Sensing (ERS) microwave scatterometer measurements to identify regions of low surface roughness. The ERS is very sensitive to surface roughness and can detect subtle changes in desert morphology [*Prigent et al.*, 2001, 2005]. We permit emission in the fraction of the grid box where the ERS backscattering is less than −13 dB, corresponding to a roughness length below 0.1 cm.

[12] Together, particle availability and surface roughness determine the susceptibility of a region to wind erosion and dust emission. This susceptibility is defined as the product of the grid box fractions permitting emission, according to the preferred source and roughness prescriptions, and is plotted in Figure 1 as a fraction of the maximum value. The lightest shade corresponds to susceptibilities below one-quarter of the maximum; the darkest corresponds to susceptibilities above three-quarters, and represents what are potentially the most productive source regions. Beneath each figure is the percentage of grid boxes in each category. For example, the most productive grid boxes represent 3.6 and 3.3% of the total in the GINOUX and ZENDER2 prescriptions, as opposed to only 1.0% in the TEGEN prescription. In the former cases, dust emission is poten-

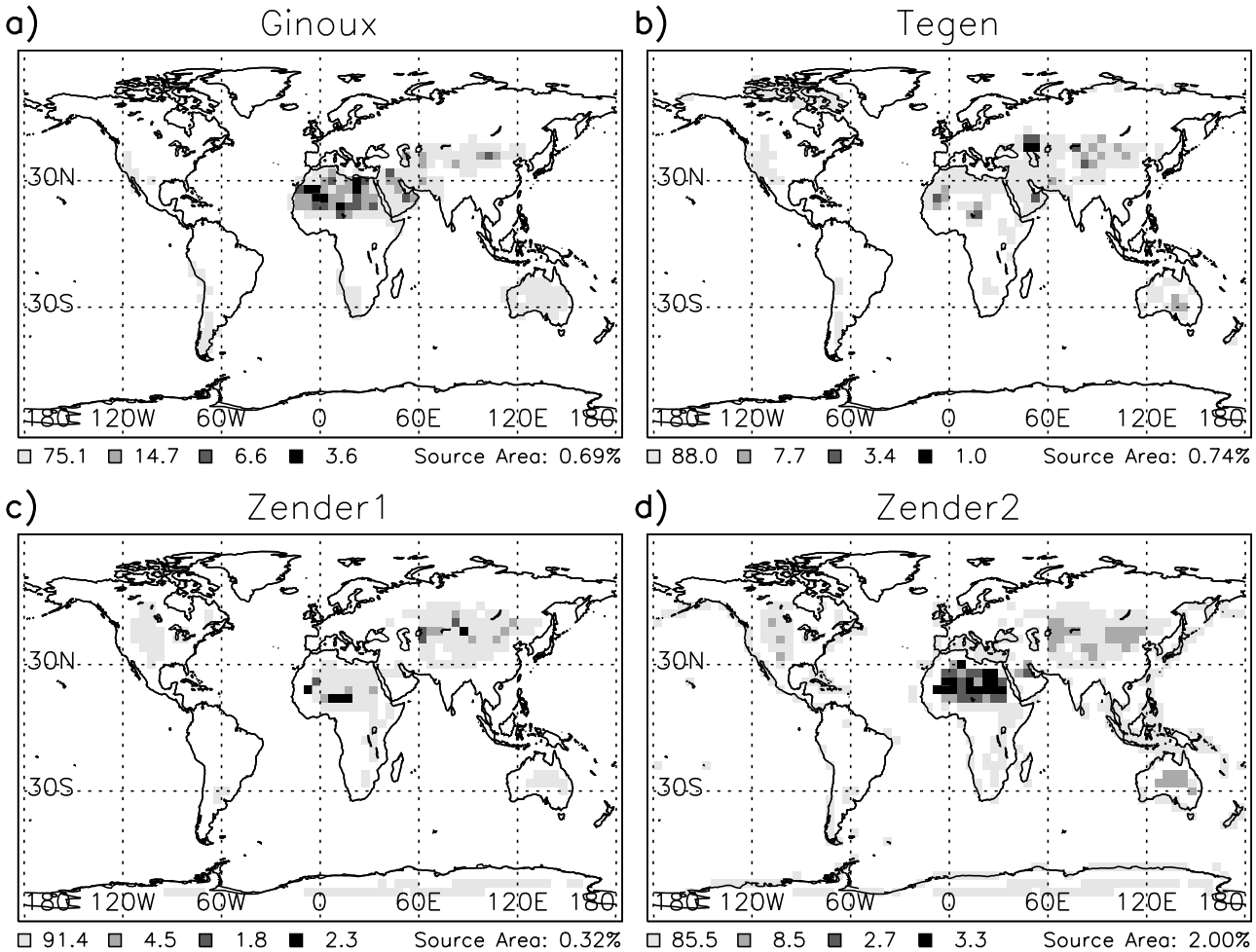

Figure 1. Susceptibility to dust emission (defined as the product of the grid box fractions identified as a preferred source and satisfying a roughness criterion), categorized as a quarterly fraction of the maximum value among all source grid boxes. The darkest squares (representing what are potentially the most prolific dust sources) correspond to susceptibility within three-quarters of the maximum; the lightest squares correspond to fractional susceptibility below one-quarter. Fractions below 0.001 are not plotted. Below each panel, the global percentage of grid boxes in each category is listed, followed by the percentage of the globe covered by dust sources. (While the susceptibility is labeled according to its preferred source prescription, it varies additionally with surface roughness.)

tially more concentrated within a few grid boxes. Also listed is the total source area as a percentage of the global surface area. In the ZENDER2 case, dust emission occurs over a total area that is roughly three times the area of emission in the GINOUX and TEGEN prescriptions. There are regional differences in susceptibility that influence where dust is emitted. Susceptibility is larger over Asia and Australia in the TEGEN prescription, compared to GINOUX, which emphasizes the Sahara. (Note that the TEGEN source has a small component based upon a conventional vegetation criterion that is not shown in Figure 1.)

[13] Saltation is observed as the main dust entrainment mechanism [*Iversen and White*, 1982; *Shao et al.*, 1993]. We assume that w_t in (1) represents the threshold for the saltating particles that are first lifted by the wind. These in turn liberate from the surface the smaller particles that remain suspended as aerosols, which we explicitly model. Although wind tunnel measurements show that dust emission increases with the surface wind stress [*Gillette*, 1978], here we use surface wind speed, which is related through the surface roughness. In essence, we are making the common approximation that the former lake beds that are prolific sources have a globally uniform roughness length. *Marticorena et al.* [1999] show that the gross features of the seasonal cycle of Saharan dust emission are represented quite well with the threshold for emission defined in terms of surface wind speed.

[14] Realistic simulation of dust emission in an AGCM is inhibited by the model's coarse resolution compared to the scale of the circulations observed to mobilize dust. Following *Cakmur et al.* [2004], we introduce a probability distribution $p(w)\,dw$ of surface wind speed within each grid box, so that (1) becomes:

$$\mathcal{E} = CF(r)\int_{w_t}^{\infty} w^2(w - w_t)\,p(w)\,dw \qquad (2)$$

Table 1. Data Used to Constrain the Dust Cycle in This Study and Its Temporal Coverage

Data Set	Reference	Period
AOT AERONET	*Holben et al.* [2001]	1990s–Present
AOT AVHRR	*Mishchenko et al.* [1999]; *Geogdzhayev et al.* [2002]	1997–2000
AOT TOMS	*Torres et al.* [2002]	1997–2000
SURFACE CONCENTRATION	*Prospero* [1996]	1980–late 1990s
DEPOSITION (DIRTMAP)	*Tegen et al.* [2002]; *Kohfeld and Harrison* [2001]	1980–mid 1990s
DEPOSITION (GINOUX)	*Ginoux et al.* [2001]	1980s
SIZE DISTRIBUTION	*Holben et al.* [2001]; *Dubovik et al.* [2002]	1990s–Present

Although the emitted fractional size distribution $F(r)$ is a function of wind speed [*Alfaro and Gomes*, 2001], we neglect this dependence for simplicity. The subgrid probability distribution $p(w)\,dw$ is calculated as in *Cakmur et al.* [2004], based upon the AGCM parameterization of PBL turbulence, along with dry and moist convection. In the AGCM, subgrid wind fluctuations are dominated by dry convection. This favors dust emission over deserts, where there is continuous mixing within the boundary layer due to intense solar heating of the surface. Given the introduction of subgrid variability, the AGCM's dust aerosol burden improves significantly compared to satellite retrievals [*Cakmur et al.*, 2004]. Through the subgrid wind speed parameterization, the AGCM identifies meteorological situations that favor dust emission. This 'preferred' meteorology complements the preferred sources of erodible particles described above.

[15] As described in section 4, separate values of the product $CF(r)$ are chosen for clay and silt to maximize model agreement with the observations. Often, $F(r)$ is specified using a global survey of soil particle size. However, this survey is typically intended for agricultural purposes [*Zobler*, 1986], and may not be the most relevant estimate of particles susceptible to erosion, which often are emitted by natural features such as dry lake beds. As noted above, $F(r)$ depends additionally upon the cascade of momentum from larger particles dislodged by the wind to the smaller aerosol particles. Because the calculation of $F(r)$ is complicated [*Grini et al.*, 2002], we derive it empirically in section 4. The effect of surface wetness upon emission is parameterized by increasing the emission threshold according to soil moisture, similar to the relationship suggested by *Shao et al.* [1996]. The resemblance of the model dust distribution to observations is fairly insensitive to the rate of threshold increase as described in greater detail by *Miller et al.* [2006]. There is no dust emission over snow or ice covered surfaces. In addition, the model assumes an unlimited availability of soil particles for emission, ignoring any possible surface crusting effects.

[16] Once the dust particles are emitted from the surface, they scatter both solar and thermal radiation and get transported by the winds. In this study, the radiative forcing is calculated as a diagnostic only and does not modify the circulation. Dust radiative forcing is calculated as described by *Tegen and Lacis* [1996] with two modifications. First, the solar absorption is reduced (through the imaginary part of the index of refraction) according to *Sinyuk et al.* [2003]. Second, optical thickness at thermal wavelengths is increased by 30% to account for the neglect of thermal scattering, as suggested by the calculations of *Dufresne et al.* [2002].

[17] Dust particles are removed from the atmosphere by both dry and wet deposition. The former is implemented according to a resistance-in-series scheme derived from the Harvard-GISS Chemical Transport Model [*Chin et al.*, 1996; *Koch et al.*, 1999, 2006]. There is no remobilization of settled dust. Wet deposition depends on the AGCM surface precipitation and removes dust according to a scavenging coefficient of 700 [*Tegen and Miller*, 1998] up to the cloud top calculated by the model.

3. Data Sets

[18] To compute an optimal dust budget by minimizing the error between the model and observations, this analysis utilizes multiple data types and a worldwide array of stations. These data sets are summarized in Table 1. The first data set consists of aerosol optical thickness (AOT) measured since the beginning of the 1990s by the Aerosol Robotic Network (AERONET), based upon CIMEL Sun/sky radiometers [*Holben et al.*, 1998; *Dubovik et al.*, 2000; *Holben et al.*, 2001]. These photometric observations are able to determine aerosol optical thickness accurately, although the aerosol species and chemical composition must be determined separately. We select AERONET stations where dust is likely to dominate the aerosol load to reduce any contribution by other aerosols, although there may be times of the year when the latter contribute significantly. We measure the sensitivity of our optimal solution to this 'contamination' in section 5.5, where we calculate the model AOT using a multi-component aerosol distribution in addition to dust.

[19] We also use AOT retrievals from the advanced very high resolution radiometer (AVHRR) from 1997 to 2000. Here the AOT is derived from a two-channel retrieval algorithm [*Mishchenko et al.*, 1999; *Geogdzhayev et al.*, 2002], which has been validated against in situ measurements at Sable Island [*Mishchenko et al.*, 2003] and long-term sun-photometer measurements over oceans [*Liu et al.*, 2004]. AOT retrievals exceeding unity are reset to this value to minimize cloud contamination, which introduces a low bias. A third measurement of AOT is provided by TOMS from 1997 to 2000 [*Torres et al.*, 2002]. The TOMS retrieval overestimates the AOT compared to other satellites and AERONET [*Myhre et al.*, 2004], but its combination with AVHRR may offset the low bias that results from the cloud screening algorithm of the latter. The optical thickness retrieved by AVHRR and TOMS are at 550 nm and 380 nm, respectively, in comparison to the 550 nm AOT measured

by AERONET and computed by the AGCM. We neglect the change of AOT between these two wavelengths. The difference is small for large dust particles, but can be larger for small far-traveled particles [*Chiapello et al.*, 2000]. In comparing to the satellite retrievals, we use regional averages because these allow a better comparison to the AGCM which computes grid box averages. Moreover, a regional comparison reduces the effect of transport errors where the AGCM winds depart from actual values. We select regions whose aerosol load is dominated by mineral dust, because the retrievals do not distinguish different aerosol species. We use the clear sky AOT computed by the model given that the satellite and surface observations of AOT are computed using a cloud masking algorithm. Additionally, the nonsphericity of dust particles introduces an uncertainty to the retrieved AOT [*Mishchenko et al.*, 1995]. This problem cannot be solved with either AVHRR or TOMS data [*Mishchenko et al.*, 2003]. Through radiance measurements at multiple wavelengths, both MODIS and Multi-angle Imaging Spectroradiometer (MISR) retrievals allow more accurate estimate of AOT and identify the aerosol type with greater confidence [*Chu et al.*, 2002; *Remer et al.*, 2002]. In addition, MISR retrieves parameters related to particle shape [*Kahn et al.*, 2001]. As these data sets extend over a longer period, they will provide a useful additional constraint on the magnitude of the dust load, although we do not include them in the present study.

[20] We use surface dust concentration measured by the University of Miami at nearly two dozen stations worldwide from the early 1980s to the late 1990s [*Savoie and Prospero*, 1977; *Prospero*, 1996]. In addition, we use sediment trap measurements of ocean deposition during the early 1980s to mid-1990s from the Dust Indicators and Records of Terrestrial and Marine Palaeoenvironments (DIRTMAP) [*Kohfeld and Harrison*, 2001]. Measurement errors in the locations of high sedimentation considered in this study are on the order of 25%, although there are additional sources of uncertainty. We use the compilation by *Tegen et al.* [2002], which selects measurements at near-uniform depths to minimize any signal by fluvial inputs or hemipelagic reworking [*Yu et al.*, 2001]. Most DIRTMAP values are based upon several seasons of measurements, although a few have records as short as 50 days. Nearby stations within the same AGCM grid box were averaged for comparison to model values, which removes some of the effect of short records. Only annual averages are compared to the model, which obviates distortion of the seasonal cycle by the lag between deposition at the ocean surface and biological transport to the sediment trap [*Bory et al.*, 2001]. Complementary deposition measurements compiled by *Ginoux et al.* [2001] provide additional data for a longer period during recent decades.

[21] Finally, we compare the size distribution retrieved by AERONET [*Dubovik and King*, 2000; *Dubovik et al.*, 2002], after interpolation to model size categories using the effective radius. Other aerosols are discernible within the accumulation mode, as indicated by the local maximum in the size distribution for radii smaller than roughly 0.2 μm [see *Miller et al.*, 2006, Figure 8]. To exclude other aerosol species, we restrict the comparison of the model and observed size distribution to particles with radii greater than 0.2 μm. A potentially larger problem is the bias between the model monthly size distribution and the observed distribution, which is restricted to dusty days with AOT greater than 0.5 in order to minimize contamination by aerosols other than dust [*Dubovik et al.*, 2002]. However, as we note in section 5.3, the optimal solution is nearly unchanged when the size distribution retrievals are excluded.

4. Methodology

[22] In order to constrain the global dust cycle we formulate a statistic Φ that represents the error between the model and the observations:

$$\Phi^2 \equiv \frac{\frac{1}{M}\sum_{i=1}^{M}\left(X_i^m - X_i^o\right)^2}{S^2}, \tag{3}$$

where S is a normalization factor:

$$S^2 = \frac{1}{2M}\left[\sum_{i=1}^{M}\left(X_i^m\right)^2 + \sum_{i=1}^{M}\left(X_i^o\right)^2\right], \tag{4}$$

X_i^o and X_i^m are the observed and modeled values, respectively, and the sum is over all M observations. The subscript i varies according to both measurement location and climatological month. The normalization S is chosen so that the errors corresponding to different data sets are of comparable order; Φ of order 1 indicates no agreement between the model and the observations.

[23] The error corresponding to individual observations is often weighted by the inverse of the observational uncertainty [*Press et al.*, 1992, chapter 15], so that more accurate observations make a larger contribution to the total error Φ and provide a stronger constraint upon the minimum value. In our case, the observations are climatological values where interannual variability typically makes a larger contribution to uncertainty than measurement error (although the latter is poorly documented). This variability generally increases with the magnitude of the observed dust load. For this reason, we decline to weight by the inverse of the uncertainty, which would have the undesired effect of emphasizing observations during the least dusty season, when measurement error is comparatively strong.

[24] Equation (3) predominantly weights stations near the source where the dust concentration is larger. This is a reasonable weighting, given that model results at far stations are influenced more strongly by the model's error in transport and deposition, which can distort the inferred emission. (For a heuristic example of how remote observations can distort the estimated emission as a result of transport and deposition errors, see Appendix B.) However, were our model applied to iron uptake by ocean biology (e.g.), which is sensitive to dust deposition in iron-limited ocean regions that are typically far from the source, a weighting which emphasizes remote stations would be more appropriate.

[25] As noted in section 2, we assign separate values of the product $CF(r)$ for clay and silt, which determine the emitted dust mass for a given distribution of wind speed (see equation (2)). We simultaneously vary the clay and silt

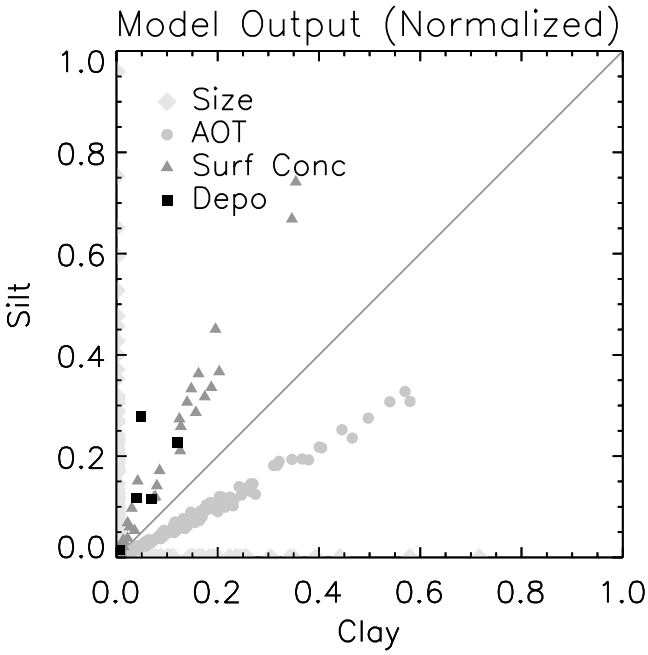

Figure 2. The contribution of clay and silt particles to model output at all observing locations. Each data set is normalized according to (A1).

values of this product (equivalent to varying clay and silt emission), and search for a minimum of the error Φ, using (3). Although emission corresponding to the minimum error can be identified using an analytic formula (as in Appendix A), our method allows us to sample the error in the neighborhood of the minimum, which reveals whether the minimum is sharply defined or part of a broad region where the error varies slowly and a wide range of emission results in nearly optimal agreement with the observations.

[26] Since there is no dust radiative feedback, the dust load increases linearly with emission. Therefore, we can vary clay and silt emission and search for the minimum error Φ given a single integration of the model. We carried out this minimization separately for each of the four preferred source functions described in section 2. Note that the observations we use as a constraint consist of many different physical quantities. Thus, while we minimize the model error by varying emission, in fact we are really constraining the entire dust cycle, including the load and deposition, rather than emission per se. One consequence is that the optimal value of emission that we derive is sensitive to uncertainties in other aspects of the dust cycle (such as AOT), whose measurements we include as a constraint.

[27] Although silt particles are transported as three separate size categories in our model, we have chosen to constrain only the total silt emission. This is because the larger silt categories make only a small contribution to the model variables that are compared against observations. Figure 2 shows the clay and silt contributions to each of these variables. (The contributions are normalized, so that different data types can be plotted together despite differing units.) Clay makes the dominant contribution to AOT, while surface concentration and deposition are dominated by silt. For each data type, the clay and silt contributions are nearly colinear. The ratio of clay to silt remains nearly unchanged as the dust plume disperses globally, even as the total concentration drops. This requires that both size categories have similar lifetimes and removal rates, indicating the absence of larger silt particles that are removed preferentially by dry deposition. Thus, the observations only weakly constrain emission of the largest silt particles, even at observing locations that are upwind and closest to the source region where the concentration is largest. By optimizing the total silt emission, we are effectively constraining the smallest silt particles, and assuming that the emitted mass in the larger categories is identical, consistent with the size distribution of emission assumed by *Tegen and Fung* [1994].

[28] Each integration is of 5 years duration, a time long enough to provide robust, statistically significant differences between experiments, but short enough to be computationally efficient. Sea surface temperature (SST) observed during the period 1997 to 2001 is used as a lower boundary condition, a period of time which overlaps with the satellite retrievals of AOT, although not necessarily with the other measurements. The use of observed SST forces the model, which controls the dust cycle, toward the observed circulation [*Bretherton and Battisti*, 2000]. Because we only carry out a single experiment for each preferred source, the correspondence of the model and observed circulation will be smaller than for an ensemble of simulations. However, the limited correspondence probably does not contribute significant uncertainty to the climatologies of the model and observation that we compare.

[29] In the next section, we derive the sensitivity of the optimal emission to different subsets of the data used to construct the error Φ. The ALL comparison makes use of all observations that have at least three years of data available. The exception is the DIRTMAP deposition data set that is available for one year at most of the locations. The ALL comparison includes some observing sites that are not downwind of any source and do not offer a strong constraint for dust. Moreover, the ALL comparison is biased toward dust sources from the Sahara more than Asia given that there are more samples downwind of the former. The RELEVANT comparison addresses this issue by weighting observations so that each source region contributes equally to the error Φ. Also, the RELEVANT case uses only those locations that are dominated by dust and have at least five years of data (except for DIRTMAP), so that the climatology is more robust. Because (3) emphasizes those stations that are closer to the source, we also consider the EQUAL case, defined in section 5.3, that gives equal emphasis for both close and far stations.

[30] Given that modelers often constrain their dust cycle to match observations in a particular region, we compare the global emission constrained by regional subsets of the data. The AFRICA experiment considers the western Sahara source and observations downwind. The ASIA experiment includes the Chinese deserts and observations over the North Pacific Ocean. The ARABIA experiment includes the Arabian Peninsula and the Arabian Sea. Both the AUSTRALIA and NAMERICA experiments are restricted to observations from the continents of Australia and North America as well as downwind oceanic regions, respectively. Finally, the BARBADOS experiment includes data only

Table 2. Locations Used in Each Experiment to Constrain the Model[a]

Location		ALL	RELEVANT	AFRICA	ASIA	ARABIA	AUSTRALIA	N. AMERICA
				AERONET				
50.5E	26.3N	Bahrain				Bahrain		
59.5W	13.2N	Barbados	Barbados	Barbados				
64.7W	32.4N							Bermuda
22.9W	16.7N	Capo Verde	Capo Verde	Capo Verde				
146.1E	34.8S						Coleambally	
17.0W	14.4N	Dakar		Dakar				
104.4E	43.6N	Dalanzadgad	Dalanzadgad		Dalanzadgad			
132.9E	12.7S						Jabiru	
155.6W	19.5N	Mauna Loa	Mauna Loa		Mauna Loa			
166.9E	0.5S	Nauru						
34.8E	31.9N	Nes Ziona				Nes Ziona		
117.9W	34.9N							Rogers Dry Lake
115.3E	32.0S						Rottnest Is.	
34.8E	30.7N	Sede Boker	Sede Boker			Sede Boker		
106.9W	34.4N	Sevilleta	Sevilleta					Sevilleta
46.4E	24.9N	Solar Village	Solar Village			Solar Village		
55.2W	5.8N	Surinam						
149.6W	17.6S	Tahiti						
111.0W	32.2N							Tucson
				AVHRR				
55–70W	12–24N	Caribbean	Caribbean	Caribbean				
15–45W	12–32N	Sub. Atlantic	Sub. Atlantic	Sub. Atlantic				
50–70W	8–24N	Arabian Sea	Arabian Sea			Arabian Sea		
				TOMS				
55–70W	12–24N	Caribbean	Caribbean	Caribbean				
15–45W	12–32N	Sub. Atlantic	Sub. Atlantic	Sub. Atlantic				
15E–25W	16–32N	Sahara	Sahara	Sahara				
50–70W	8–24N	Arabian Sea	Arabian Sea			Arabian Sea		
				SURFACE CONCENTRATION				
59.5W	13.2N	Barbados	Barbados	Barbados				
64.7W	32.4N	Bermuda						Bermuda
52.3W	4.9N	Cayenne						
126.5E	33.5N	Cheju	Cheju		Cheju			
162.3E	11.3N	Enewetak						
159.3W	3.9N	Fanning						
179.2W	8.5S	Funafuti						
128.3E	26.9N	Hedo						
20.3W	63.4N	Heimaey						
16.5W	28.3N	Izaña	Izaña	Izaña				
9.9W	53.3N	Mace Head						
80.3W	25.8N	Miami	Miami	Miami				
177.4W	28.2N	Midway	Midway		Midway			
167.0E	0.5S	Nauru						
168.0E	29.1S	Norfolk Is.					Norfolk Is.	
157.7W	21.3N	Oahu	Oahu		Oahu			
159.8W	21.3S	Rarotonga						
170.6W	14.3S	Samoa						
167.0E	22.2S	Yate					Yate	
				DEPOSITION (GINOUX)				
162.3E	11.3N	Enewetak						
159.3W	3.9N	Fanning						
6.5E	45.5N	French Alps						
177.4W	28.2N	Midway	Midway		Midway			
167.0E	0.5S	Nauru						
167.0E	22.2S	New Caledonia					New Caledonia	
172.8E	34.5S						New Zealand	
168.0E	29.1S	Norfolk Is.					Norfolk Is.	
157.7W	21.3N	Oahu	Oahu		Oahu			
159.8W	21.3S	Rarotonga						
174.1E	52.9N	Shemya						
2.3E	41.8N	Spain						

Table 2. (continued)

Location		ALL	RELEVANT	AFRICA	ASIA	ARABIA	AUSTRALIA	N. AMERICA
				DIRTMAP				
		48 Sites	10 Sites	12 Sites	5 Sites	4 Sites	3 Sites	
				SIZE DISTRIBUTION				
50.5E	26.3N	Bahrain				Bahrain		
59.5W	13.2N	Barbados	Barbados	Barbados				
64.7W	32.4N							Bermuda
22.9W	16.7N	Capo Verde	Capo Verde	Capo Verde				
17.0W	14.4N	Dakar		Dakar				
104.4E	43.6N	Dalanzadgad	Dalanzadgad		Dalanzadgad			
34.5E	30.5N	Sede Boker	Sede Boker			Sede Boker		

[a]The BARBADOS experiment uses only Barbados station data and the Caribbean regional average for the satellite retrievals.

from this island along with satellite retrievals of Caribbean AOT. The locations used to constrain the model in each experiment are listed in Table 2 and in Figure 3.

5. Results

5.1. Optimal Dust Distribution

[31] Before showing how each data set constrains the optimal dust cycle, we present an example of the aerosol load that results from this optimization. A more extensive, regional comparison of the optimal dust cycle to each data set is presented in *Miller et al.* [2006]. The optimal aerosol load calculated using the GINOUX source is shown in Figure 4. The optimal case is identified using the combination of data sets listed in Table 1, and measurement locations listed in Table 2, as described in section 5.3. In order that each source region influence the optimal solution equally, we use the weights corresponding to the RELEVANT case. Figure 4 shows an aerosol plume extending across the Atlantic from North Africa during most seasons. Saharan dust is transported over the Cape Verde Islands throughout the year, while easterly trade winds during the winter bring additional dust from the Sahel [*Chiapello et al.*, 1995]. As the Northern Hemisphere (NH) summer approaches and the Intertropical Convergence Zone moves northward, the Trade winds that transport the dust shift poleward as well, so that AOT peaks at a higher latitude during this season [*Swap et al.*, 1996]. Near the coast of eastern Asia, during the NH spring, there is a plume extending into the Sea of China and North Pacific, associated with dust transported from the Taklimakan and Gobi deserts. There is also dust over the Australian continent during the Southern Hemisphere (SH) summer, which is the active dust season in this region [*Prospero et al.*, 2002]. The global, annual-average load is dominated by silt particles, at 18.6 Tg versus 5.0 Tg for clay, as shown for the 'RELEVANT' case in Figure 5.

5.2. Error Φ for Individual Data Sets

[32] We calculate the optimal dust distribution identified by each data set using the GINOUX preferred source prescription and the RELEVANT subset of observations.

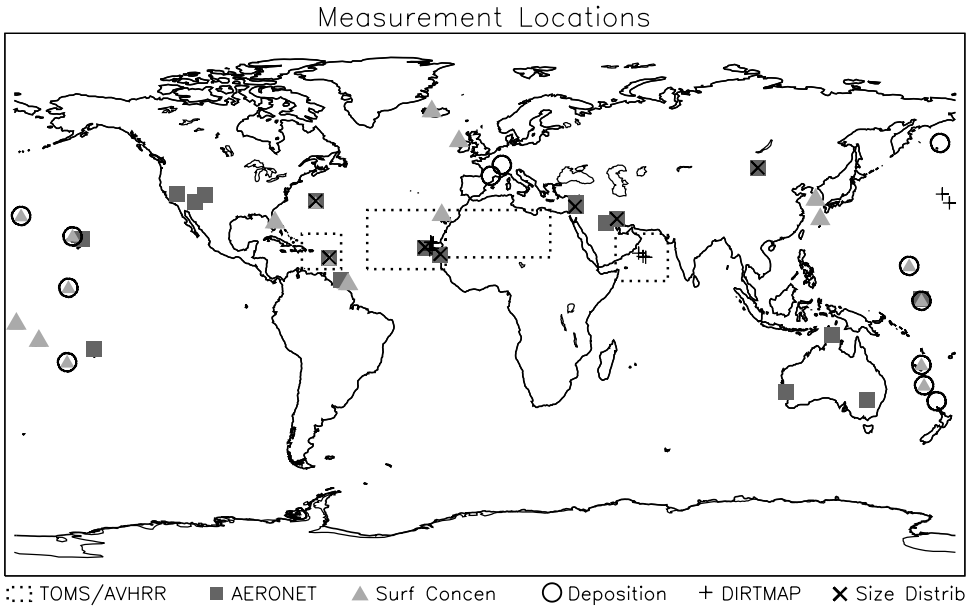

Figure 3. The locations and regions used to constrain the model. The dotted regions indicate the domain for areal averages of the satellite retrievals. The square is AERONET, the triangle is Miami surface concentration, the circle is Ginoux deposition, the plus is DIRTMAP, and the cross is AERONET size distribution.

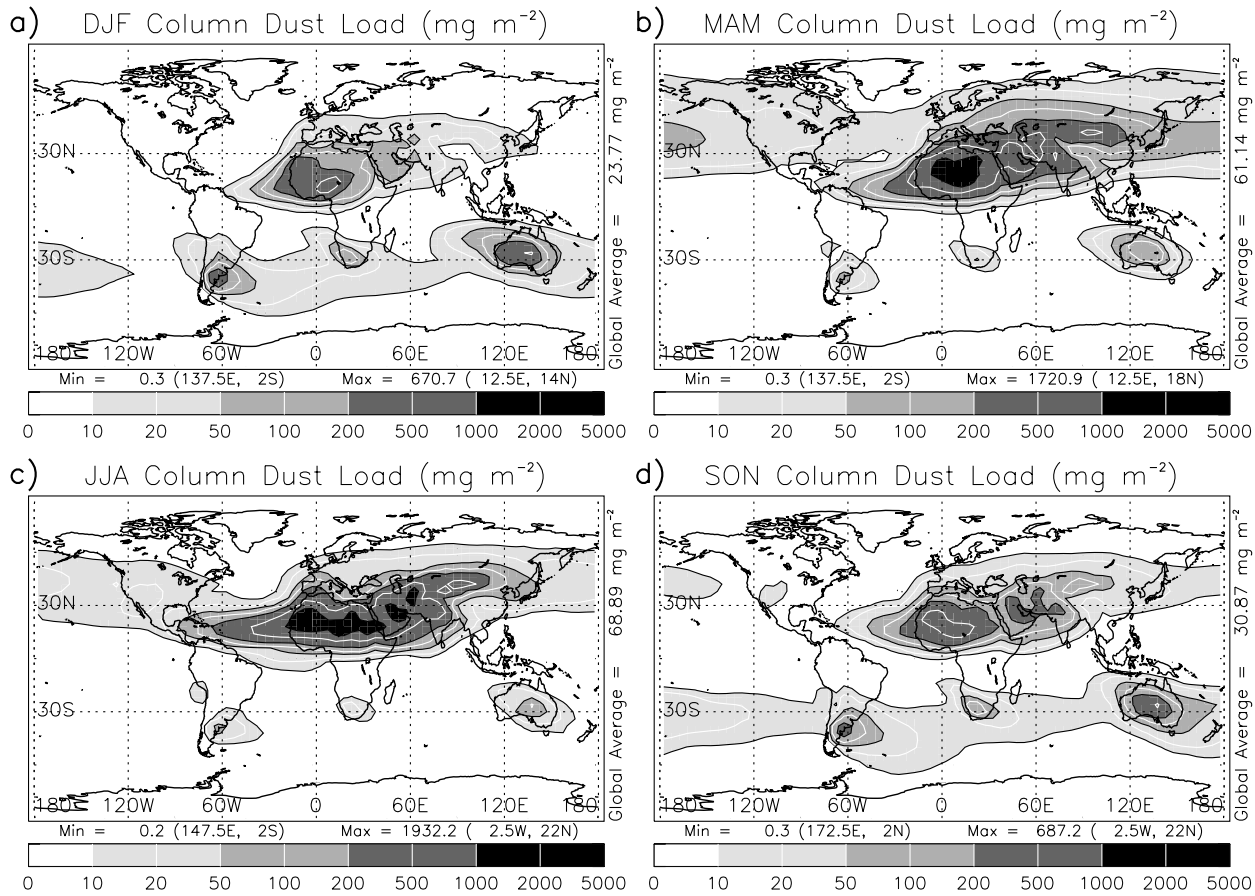

Figure 4. Column dust load (mg m^{-2}) for (a) DJF, (b) MAM, (c) JJA, and (d) SON.

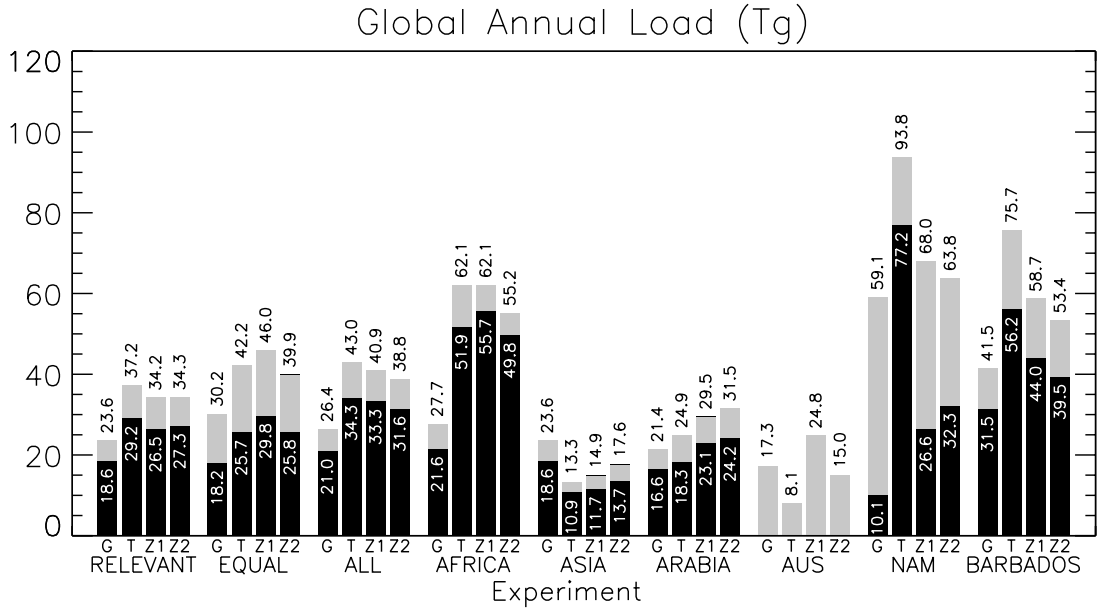

Figure 5. The optimal global dust load for each experiment (annual average). The light and dark shading shows the optimal clay and silt load, respectively. The number above each bar is the optimal total load. The optimal silt value is also given where it is non-zero, and the clay load is the difference with respect to the total. Each of the nine experiments are subdivided according to the preferred source prescription, where G is GINOUX, T is TEGEN, Z1 is ZENDER1, and Z2 is ZENDER2. The experiments AUS and NAM are AUSTRALIA and NORTH AMERICA, respectively.

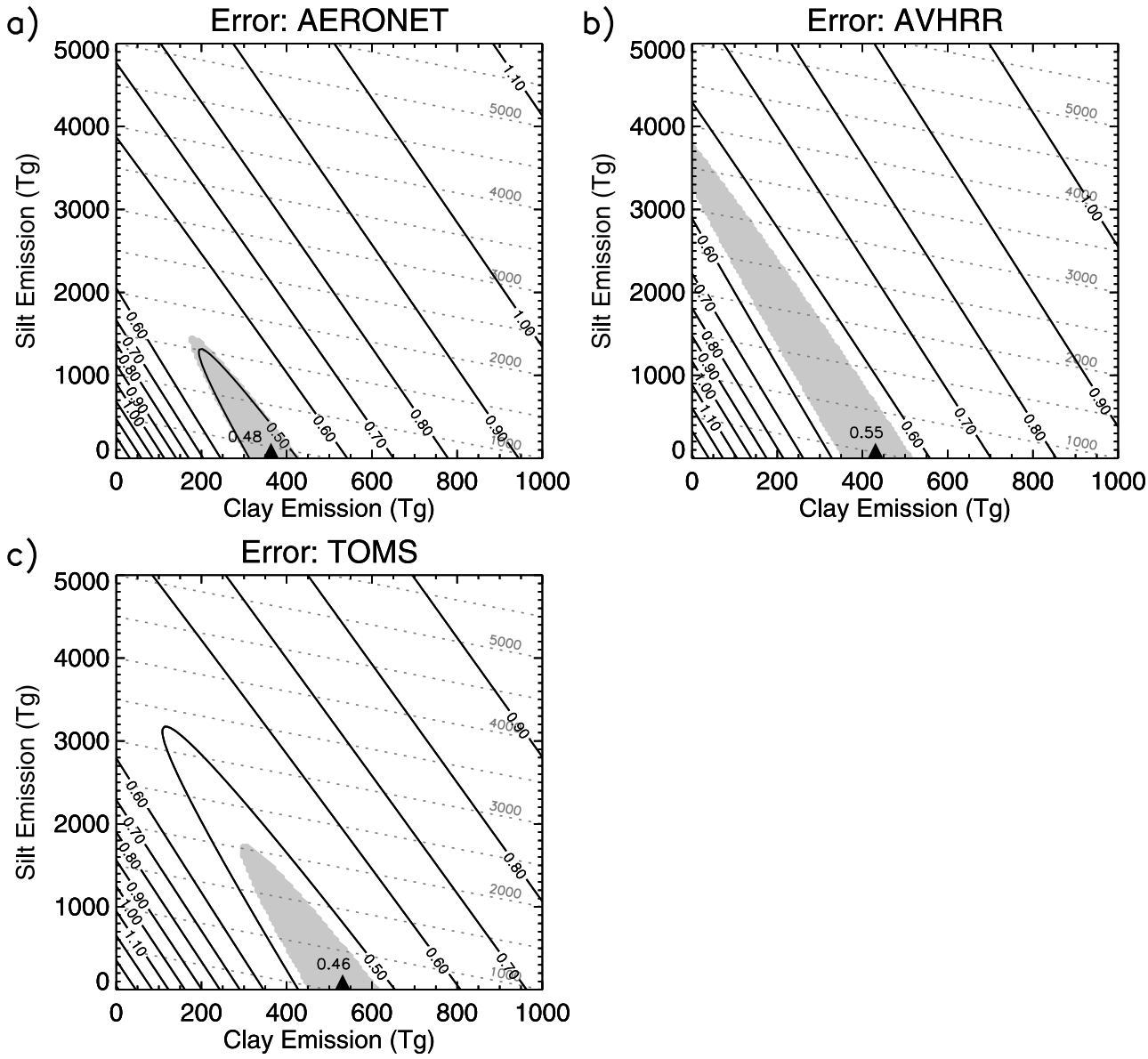

Figure 6. Model error Φ (solid contours), according to (a) AERONET, (b) AVHRR, and (c) TOMS AOT for the RELEVANT experiment using the GINOUX source. The dotted lines mark total emission. The optimal value is marked by the black triangle. The shading indicates values of the error Φ that are within 5% of the minimum.

Figure 6 shows the error Φ based upon AOT observations from AERONET, AVHRR, and TOMS. Each panel shows contours of the error (denoted by solid lines) as clay and silt emission are varied along the horizontal and vertical axis, respectively. The dotted lines represent total emission. The optimal value indicated by each individual data set is given by the minimum in the error Φ and is marked by the black triangle. This figure shows that the optimal annual emission for all three AOT data sets is around 450 Tg of clay without any silt emission.

[33] A number of factors contribute to uncertainty in our estimate of the optimal emission. The observations are subject to measurement error and their climatology is uncertain due to interannual variability. We estimate the latter in Appendix A. Below, we estimate the effect of our subjective selection of observing stations and data types upon the optimal solution by considering different combinations. Because these combinations are not exhaustive, we also shade Figure 6 in the vicinity of the optimal solution to indicate values of the error Φ that are within 5% of the minimum. This criterion is arbitrary. Nonetheless, emission within the shaded region is only slightly less consistent with the observations than the optimal solution.

[34] Both surface concentration from the University of Miami and deposition from DIRTMAP indicate that the optimal distribution corresponds mostly to silt emission with little clay (Figure 7). Their optimal values are approximately 1,600 Tg. The deposition compiled by Ginoux constrains the optimal emission to consist entirely of clay (Figure 7b). The unusually small error and restricted range of the optimal solution for this data set may stem from the fact that only two locations satisfy the RELEVANT criterion

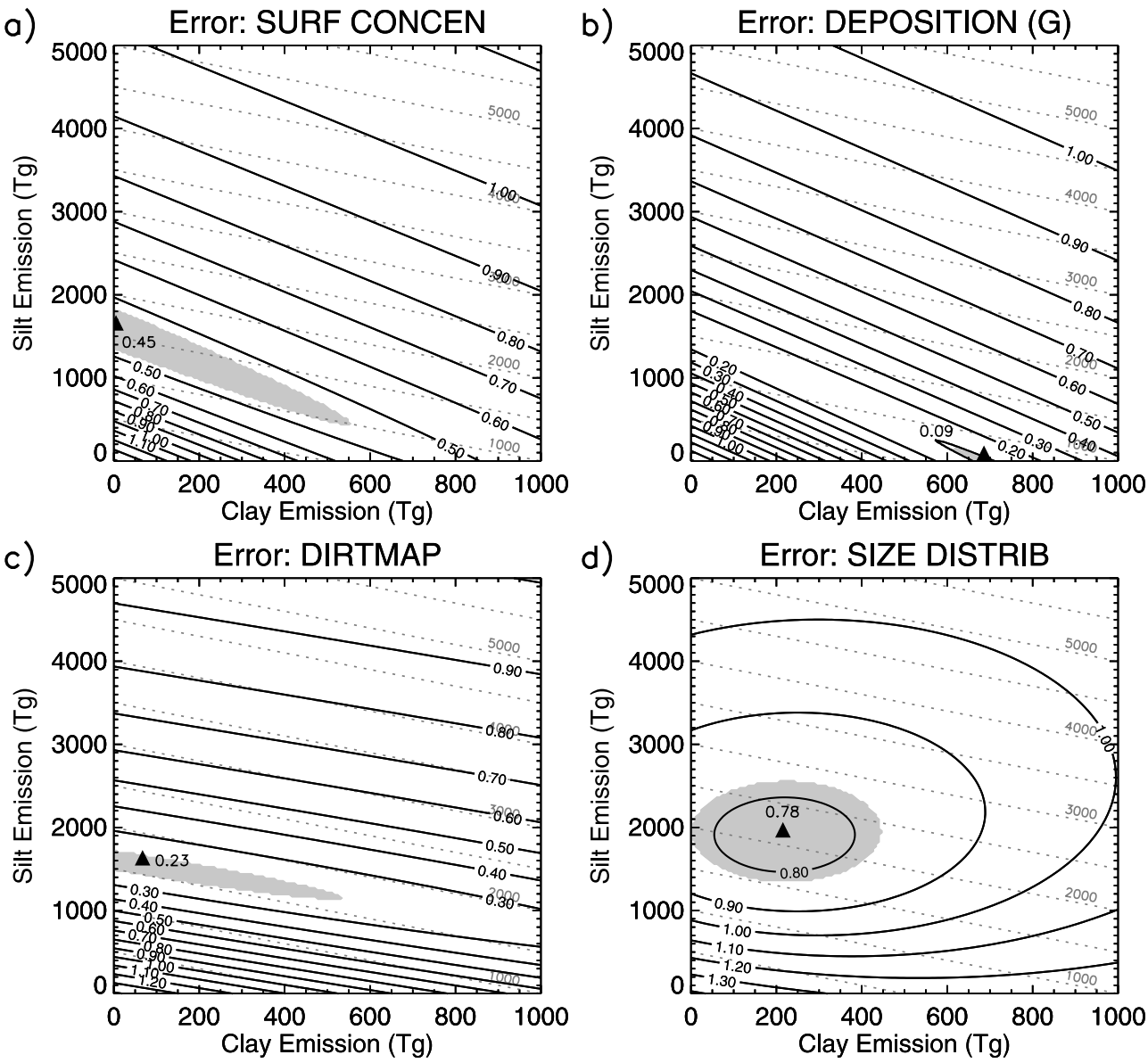

Figure 7. As in Figure 6, according to (a) University of Miami surface concentration, (b) Ginoux deposition, (c) DIRTMAP deposition, and (d) AERONET size distribution.

of containing at least 5 years of measurements (Table 2). The model can match the observations closely at these two locations, despite unrealistic behavior elsewhere that is not penalized. Only the size distribution indicates non-zero optimal values of both clay and silt simultaneously (Figure 7d). It indicates an annual optimal emission of around 2,100 Tg, with 200 Tg from clay and 1,900 Tg from silt.

5.3. Error Φ_T for Combined Data Sets

[35] Here, we compute the consensus optimal emission by minimizing the error constructed from all seven data sets listed in Table 1. For each data set (denoted by j) we calculate the root mean square error Φ_j according to (3). Then the total or combined error Φ_T is:

$$\Phi_T = \sum_{j=1}^{7} w_j \Phi_j \tag{5}$$

where the weights w_j assigned to each data set sum to unity. We allow observations of AOT, surface concentration, deposition and size distribution to contribute equally to the total error. Because there are two deposition data sets, each is weighted half as much compared to surface concentration. We also decide somewhat arbitrarily to weight AERONET measurements of AOT twice as much as the TOMS and AVHRR retrievals. Our weights for each data set are given in Table 3.

[36] The optimal emission that minimizes the total error Φ_T is listed for various experiments in Figure 8. For the GINOUX source (and RELEVANT set of observations), the optimal annual emission is 1,534 Tg, comprised of 188 and 1,345 Tg of clay and silt emission, respectively. This is in the middle range of global emission calculated by other dust models [*Ginoux et al.*, 2001; *Tegen et al.*, 2002; *Mahowald et al.*, 2002; *Zender et al.*, 2004]. However, our model requires higher values of emission to match the observations

Table 3. Weighting of Each Individual Data Set Used to Compute the Total Error in Equation (5)

Experiment	AERONET	AVHRR	TOMS	SURF[a]	DEPO (G)[b]	DIRTMAP	SIZE[c]
ALL	1/8	1/16	1/16	1/4	1/8	1/8	1/4
RELEVANT	1/8	1/16	1/16	1/4	1/8	1/8	1/4
AFRICA	1/8	1/16	1/16	1/4	0	1/4	1/4
ASIA	1/4	0	0	1/4	1/8	1/8	1/4
ARABIA	1/6	1/12	1/12	0	0	1/3	1/3
AUSTRALIA	1/3	0	0	1/3	1/6	1/6	0
N. AMERICA	1/3	0	0	1/3	0	0	1/3
BARBADOS	1/6	1/12	1/12	1/3	0	0	1/3

[a]University of Miami surface concentration.
[b]Deposition compiled by *Ginoux et al.* [2001].
[c]AERONET size distribution.

when other source prescriptions are used. Optimal emission for all other sources exceeds 2200 Tg and for the TEGEN source is as high as 2600 Tg (Figure 8). The contribution of each region to the global optimal emission is listed in Figure 9. Global emission is greater with the TEGEN source compared to GINOUX as a result of greater emission over Australia and Central Asia, as anticipated from the erosion susceptibility associated with each source prescription (Figure 1). Note that due to their short observing record, no locations near Australia constrain the optimal dust cycle in the RELEVANT case. (We include constraints upon Australian emission in section 5.4.)

[37] The error Φ with respect to each data set resulting from the consensus optimal solution is listed in Table 4. (The errors are calculated for each source prescription, but for the GINOUX case, the error can also be derived from Figures 6 and 7 using the optimal clay and silt emission identified in Figure 8.) The error associated with the consensus optimal solution is roughly comparable for each individual data set. The exception is the size distribution retrievals, where the resemblance is slightly worse.

[38] Clay makes a much smaller contribution than silt to the optimal emission listed in Figure 8. For the RELEVANT case, clay contributes between 12 and 14% of the total, depending upon the source prescription. Clay also makes a relatively small contribution to the global load, according to Figure 5. For the RELEVANT case, the proportion of silt to clay ranges from 3.4 to 4.0 parts, depending upon the source. These values are substantially higher than the silt proportion in other current models, which range from 0.4 to 1.6 [*Miller et al.*, 2004, Table 1]. Although the possibility that current models underestimate silt emission has been suggested previously by the size distribution observed during the Puerto Rico Dust Experiment (PRIDE [*Reid et al.*, 2003; *Maring et al.*, 2003]), the optimal fraction of silt remains large even if the size distribution is excluded from the optimization (see below). The large silt proportion compared to other models results from optimizing the model with different observing sites and data sets.

[39] Figure 10 shows the total error Φ_T as a function of clay and silt emission. For all but one source prescription, the minimum error is not sharply defined; global emission as large as 3500 Tg corresponds to an error that is within 5% of the actual minimum. This suggests that the optimal emission may be sensitive to modest changes to our choice of observations or our definition of the error. If we use all

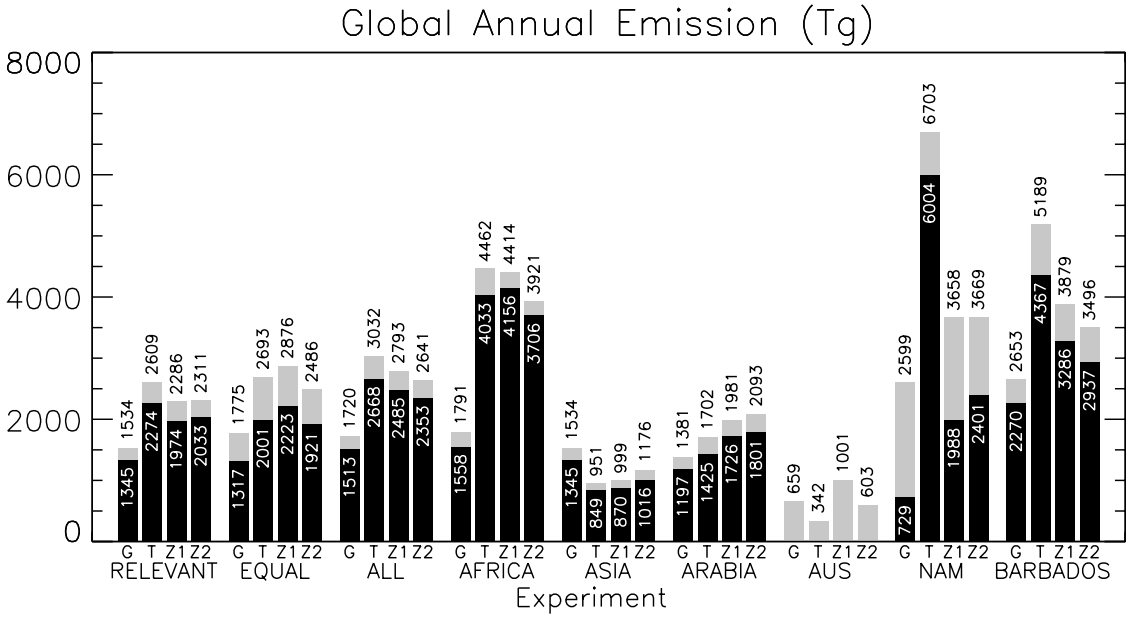

Figure 8. As in Figure 5, but for global annual emission.

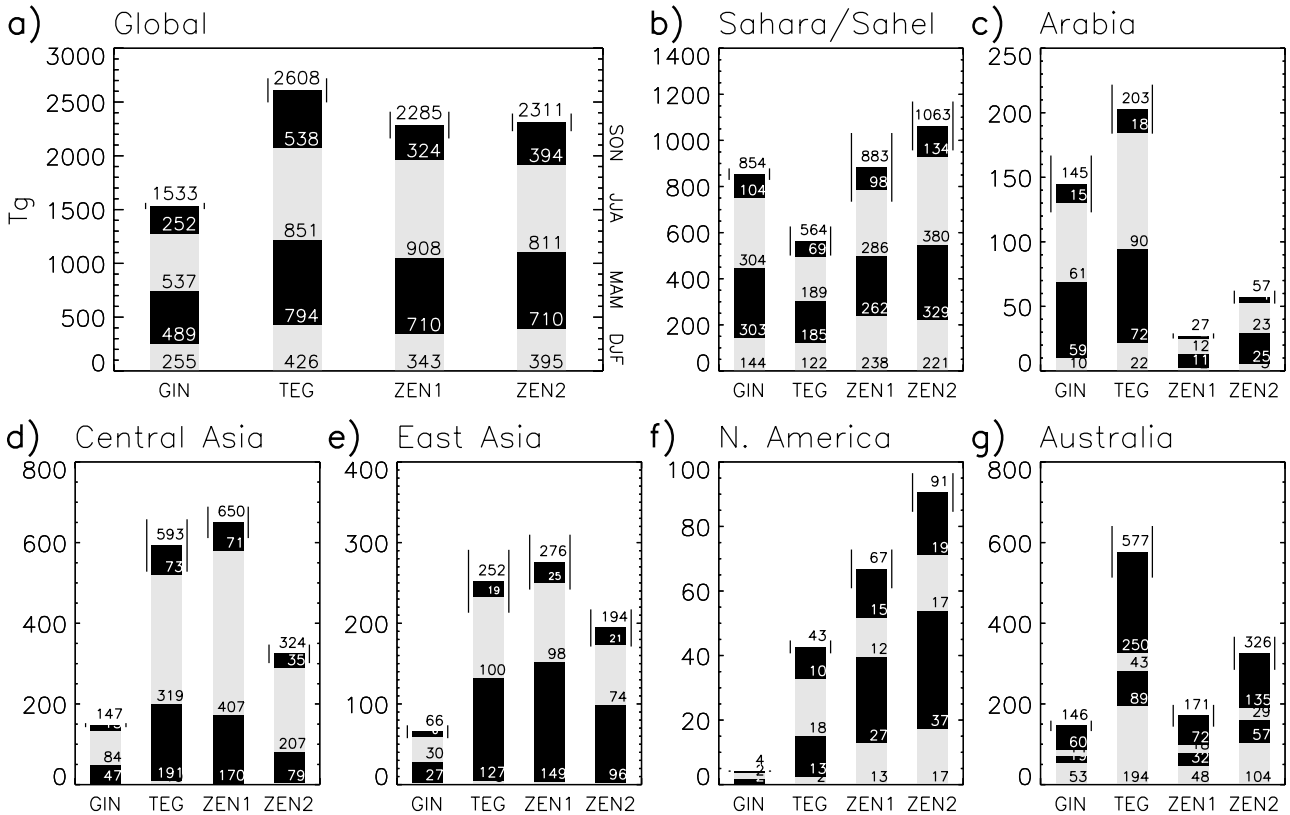

Figure 9. Regional emission of soil dust aerosol (Tg), for the globally optimal RELEVANT solution. The experiments with the GINOUX, TEGEN, ZENDER1, and ZENDER2 sources are denoted by GIN, TEG, ZEN1, and ZEN2, respectively. Each bar is divided into seasonal totals for DJF (bottom, light), MAM (above, dark), JJA (above, light), and SON (top, dark). The annual total is given at the top of each bar. The vertical lines bracketing the annual average range between one standard deviation above and below. The Sahara/Sahel average consists of Northern Hemisphere Africa grid boxes. Central Asia is defined between 25–90°E, 32–53°N; and Arabia between 35–60°E (but east of the Red Sea) and 12–36°N.

Table 4. Total Error and Error With Respect to Each Data Set, Corresponding to the Consensus Optimal Solution Calculated Using All Data Sets

Preferred Source	AERO	AVHRR	TOMS	SURF[a]	DEPO (G)[b]	DIRTMAP	SIZE[c]	TOTAL[d]
				RELEVANT				
Ginoux	0.50	0.59	0.59	0.47	0.18	0.23	0.82	0.51 ± 0.22
Tegen	0.70	0.57	0.65	0.47	0.85	0.49	0.98	0.69 ± 0.21
Zender1	0.73	0.56	0.64	0.66	0.74	0.89	0.95	0.77 ± 0.13
Zender2	0.55	0.56	0.56	0.48	0.69	0.60	0.86	0.64 ± 0.15
				ALL				
Ginoux	0.53	0.57	0.54	0.72	0.53	0.40	0.76	0.62 ± 0.13
Tegen	0.69	0.57	0.58	0.74	0.80	0.62	0.91	0.75 ± 0.13
Zender1	0.72	0.56	0.58	0.81	0.62	0.87	0.88	0.77 ± 0.11
Zender2	0.55	0.55	0.52	0.71	0.59	0.65	0.77	0.66 ± 0.09
				EQUAL				
Ginoux	0.66	0.69	0.65	0.68	0.26	0.51	0.79	0.63 ± 0.16
Tegen	0.63	0.69	0.66	0.63	0.73	0.37	0.82	0.66 ± 0.13
Zender1	0.59	0.63	0.62	0.63	0.71	0.47	0.80	0.66 ± 0.10
Zender2	0.56	0.63	0.63	0.59	0.61	0.39	0.78	0.62 ± 0.12

[a]University of Miami surface concentration.
[b]Deposition compiled by *Ginoux et al.* [2001].
[c]AERONET size distribution.
[d]The total error plus or minus the standard deviation with respect to the individual data sets.

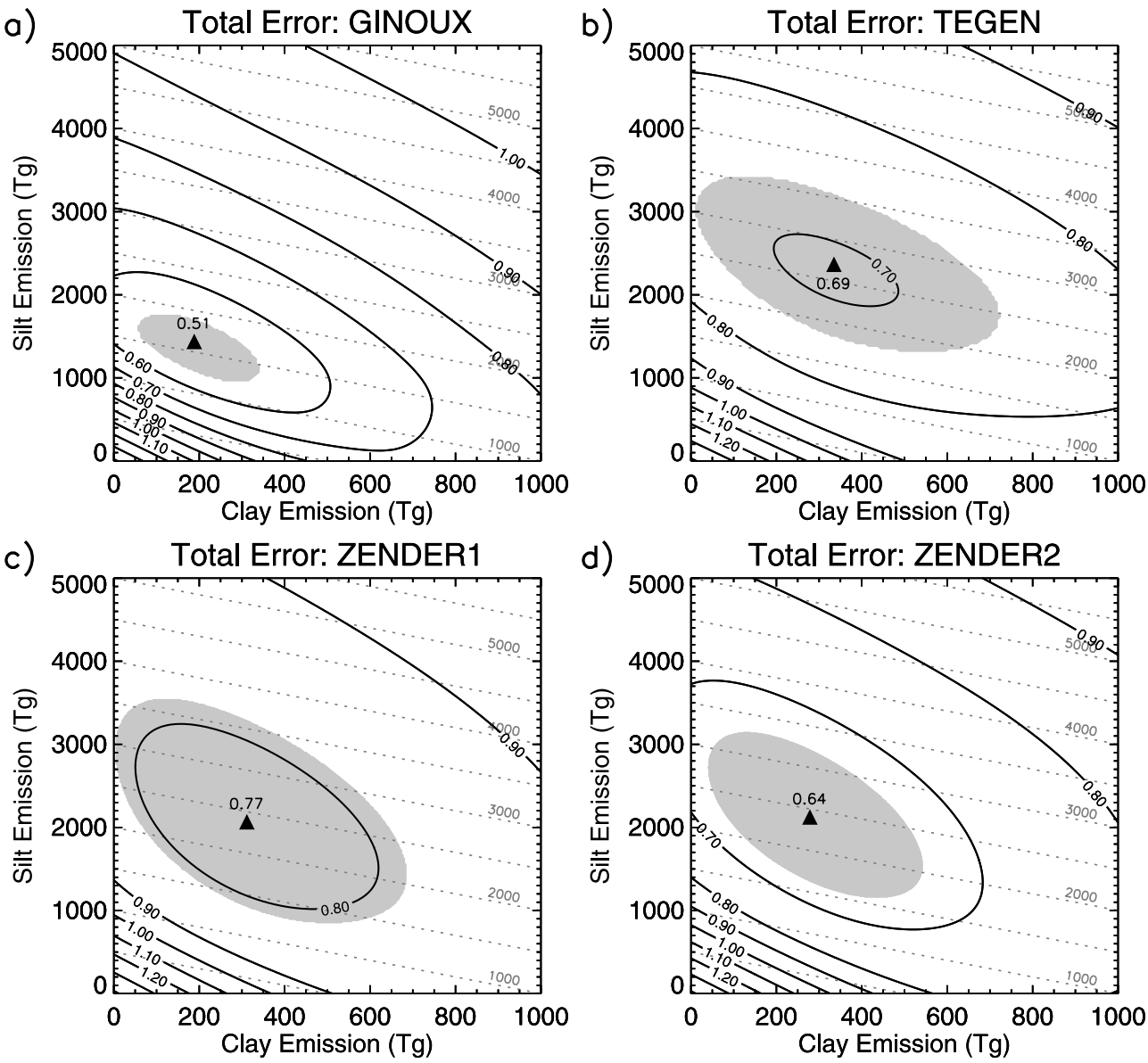

Figure 10. As in Figure 6, but for the total error based upon the (a) GINOUX, (b) TEGEN, (c) ZENDER1, and (d) ZENDER2 preferred source prescriptions.

available observations (the ALL experiment defined in section 4), including those in non-dusty locations, then Figure 8 shows that the optimal global emission rises by a few hundred Tg compared to the RELEVANT case.

[40] In the RELEVANT experiment, upwind stations, where the dust concentration is highest, have the greatest potential influence upon the error (3). As an alternative weighting, we redefine the error Φ so that each observation has the same potential to contribute (the EQUAL experiment). We recompute the error Φ by normalizing so that the error at each station is of the same potential magnitude:

$$\Phi^2 \equiv \frac{1}{2M}\sum_i^M \left[\frac{\left(X_i^m - X_i^o\right)}{\frac{1}{2}\left(X_i^m + X_i^o\right)}\right]^2 \qquad (6)$$

The denominator ensures that Φ is non-dimensional, and that stations with the same fractional error make a similar contribution to the error Φ, even if there is a large difference in concentration between the stations. For all source prescriptions, the total error remains nearly unchanged (Table 4), but the optimal emission increases by a few hundred Tg compared to the RELEVANT case, especially the emission of clay particles (Figure 8). For the GINOUX source, the optimal clay emission in the EQUAL case is 460 Tg/yr, more than twice the estimate from the RELEVANT case. By allowing observations with the same fractional error to make similar contributions to the error Φ, we give increased emphasis to stations where the load is dominated by clay particles due to the large distance from the source region. The increase in clay emission needed to match the observations at distant stations suggests that dust transport might be too slow, or that the model's wet deposition (which is the primary removal mechanism of clay) is too high. Nonetheless, we argue in Appendix B that stations near the source are a better constraint upon

Table 5. Optimal Emission $\mathcal{E}$ With Individual Contributions From Clay $\mathcal{E}_c$ and Silt $\mathcal{E}_s$, When a Single Data Set is Excluded From the Calculation of the Minimum Total Error Φ_T

Excluded Data	$\mathcal{E}$	$\mathcal{E}_c$	$\mathcal{E}_s$	Φ_T
AOT (AERONET)	1546	229	1317	0.52
AOT (AVHRR)	1547	202	1345	0.51
AOT (TOMS)	1527	182	1345	0.51
Surface Concentration	1596	195	1401	0.52
Deposition (Ginoux)	1631	202	1429	0.51
Deposition (DIRTMAP)	1386	209	1177	0.50
Size (AERONET)	1406	229	1177	0.40

emission, because their agreement with the model is not distorted by errors in transport or deposition.

[41] As an additional sensitivity test, we remove one data set from the calculation of the total error Φ_T, before computing the optimal solution. Table 5 shows that for the GINOUX source and RELEVANT set of locations, total emission ranges from 1406 Tg, when AERONET size retrievals are excluded, to 1631 Tg in the absence of the deposition measurements compiled by Ginoux. Total emission remains within roughly 10% of the 1534 Tg computed using all data sets. This variation is small compared to the range of optimal emission computed using a single data set (shown in Figures 6 and 7), demonstrating that the combination of data sets results in a much more robust estimate. While the total emission can either increase or decrease due to exclusion of a single data set, clay emission increases in all but one case, although by no more than roughly 20%.

[42] Modelers often constrain their dust model to match observations in a single region. Here, we recompute the global optimal emission using observations downwind of a single region. Not all the data sets are available in each region (Table 2). For instance, deposition compiled by Ginoux is unavailable downwind of AFRICA, and satellite retrievals of AOT are missing downwind of ASIA due to persistent cloud cover. In an effort to compensate, we accept stations where the climatology is shorter than the five years required for inclusion in the RELEVANT case. These additional stations are listed in Table 2. Figure 8 shows that global emission is very sensitive when constrained by observations from only a single region. For the TEGEN and ZENDER preferred sources, for example, global emission varies by more than threefold depending upon whether it is constrained using observations from Africa or Asia.

5.4. Regional Optimization

[43] So far, we have used observations to constrain the global value of C in (2) along with the emitted fraction of clay and silt particles. These parameters presumably have regional variations, reflecting variations in the distribution of soil particle size, for example. In this section we constrain these parameters for each major source region separately. For example, we use observations from locations downwind of Africa to optimize emission only for African sources. (In contrast, in the AFRICA case in the previous section, we used locations downwind of Africa to optimize

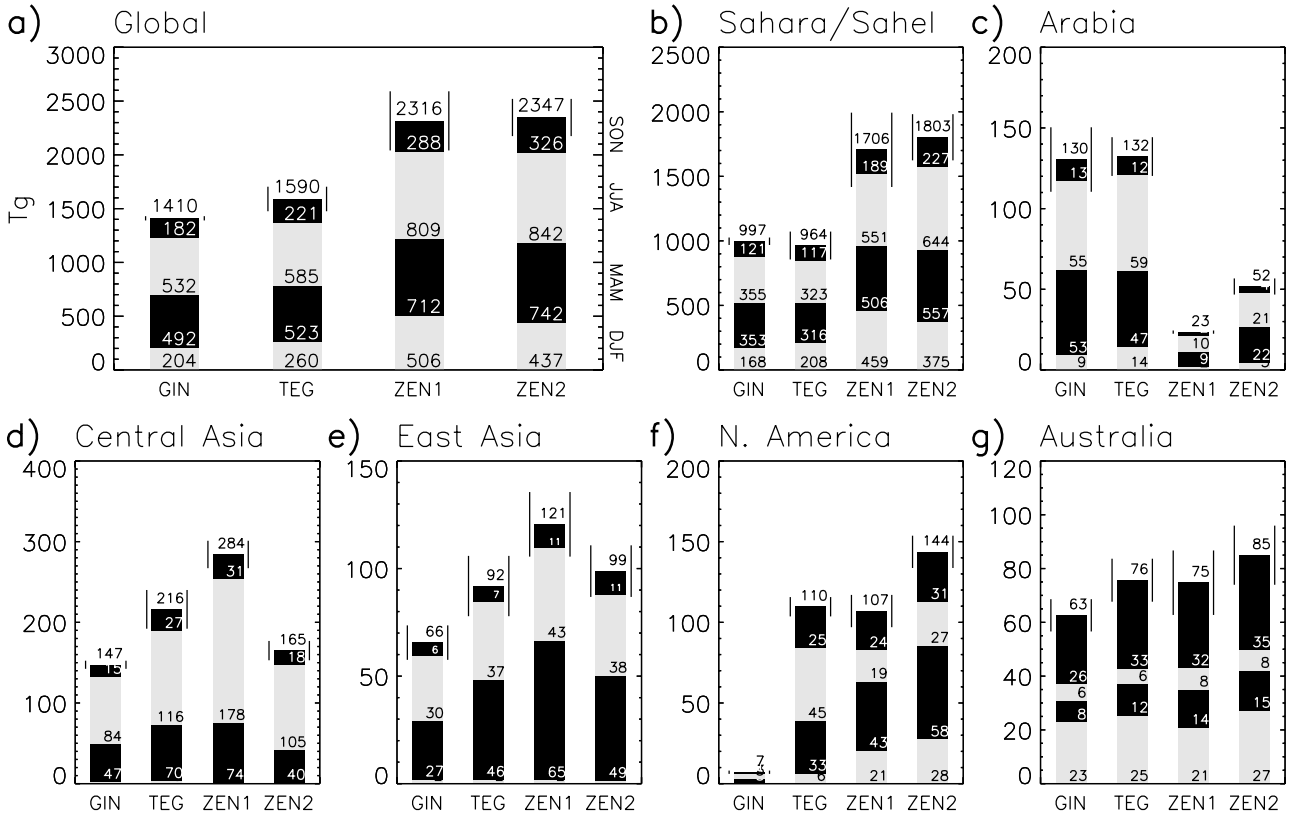

Figure 11. As in Figure 9, but for optimal emission derived by constraining the dust cycle for each region separately.

Table 6. Optimal Value of C (Normalized by the Global Optimal Value at the Bottom) and the Ratio of Silt Emission $\mathcal{E}_s$ to Clay Emission $\mathcal{E}_c$ for Each Region[a]

	GINOUX		TEGEN		ZENDER1		ZENDER2	
Experiment	C	$\mathcal{E}_s/\mathcal{E}_c$	C	$\mathcal{E}_s/\mathcal{E}_c$	C	$\mathcal{E}_s/\mathcal{E}_c$	C	$\mathcal{E}_s/\mathcal{E}_c$
			Regional					
AFRICA	1.17	6.7	1.71	9.4	1.93	16.1	1.70	17.2
CENTRAL ASIA	1.00	7.2	0.36	8.4	0.44	6.7	0.51	6.5
EAST ASIA	1.00	7.3	0.36	8.2	0.44	6.6	0.51	6.5
ARABIA	0.90	6.6	0.65	5.0	0.87	6.7	0.91	6.4
AUSTRALIA	0.43	0	0.13	0	0.44	0	0.26	0
NAMERICA	1.69	0.4	2.57	8.9	1.60	1.2	1.59	1.9
			Global[b]					
	9.71	7.1	15.27	6.8	29.37	6.3	5.12	7.3

[a]Optimization of each region uses only sources downwind of that region.
[b]For the global case (Figure 10), C is not normalized and has units of kg s^2/m^5.

global emission.) Note that constraining the model with observations not only constrains poorly-known parameters but has the unfortunate effect of compensating for model errors. This effect becomes more problematic as we increase the number of regions.

[44] Figure 11 shows the optimal emission for each region when constrained only by observing sites that are downwind. For the GINOUX and TEGEN sources, the global sums based upon constraining each region independently are in much better agreement than when emission is constrained globally (see Figure 9). To a certain extent, this increased agreement is because constraining each region separately compensates for regional differences in the source prescriptions. For example, in the RELEVANT experiment, the TEGEN source is substantially more productive than the GINOUX source over Australia, while the GINOUX source is more productive over Africa (Figure 9).

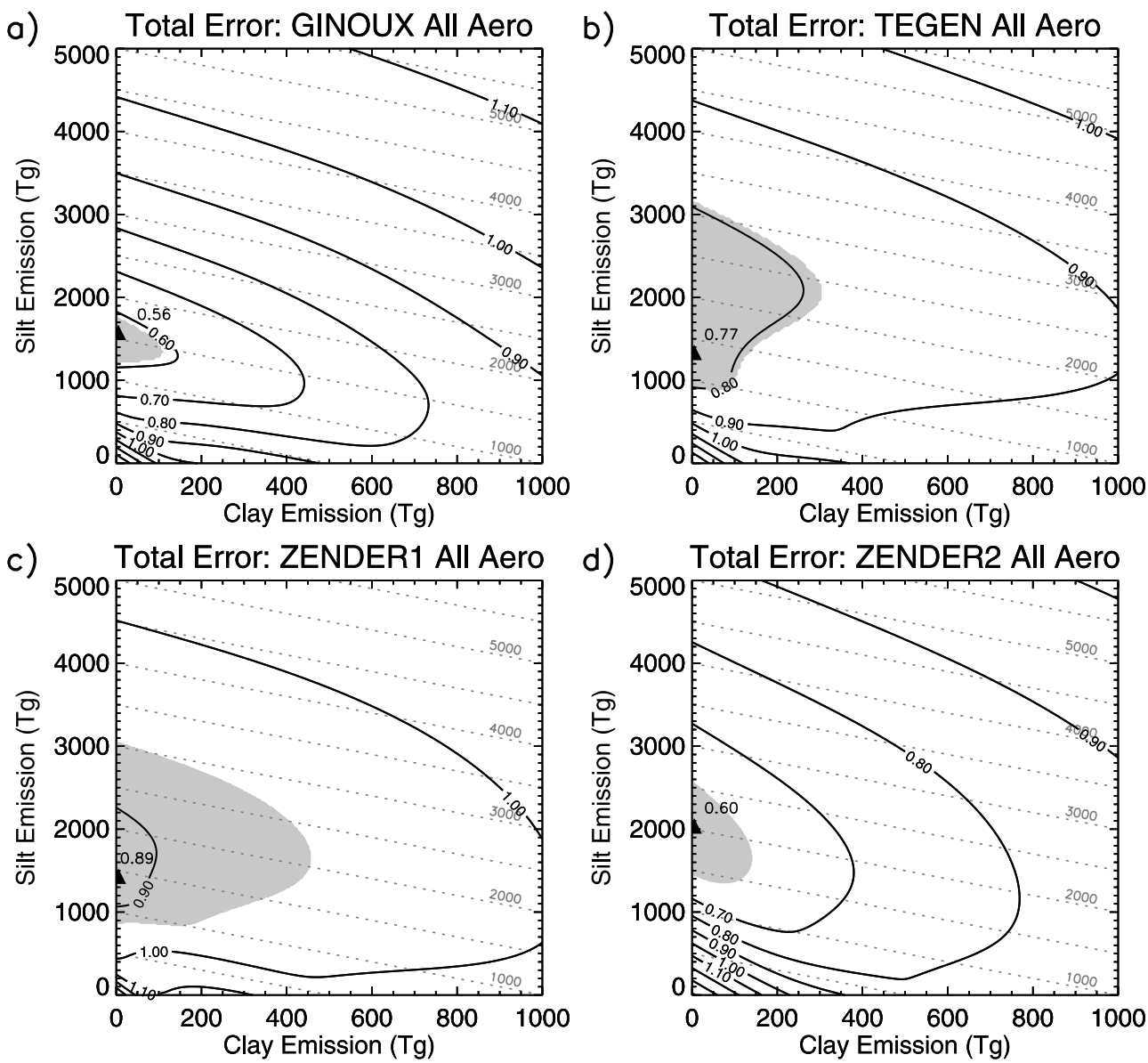

Figure 12. As in Figure 10, but including contributions to AOT from model estimates of sulfate and sea salt, along with black and organic carbon, in addition to dust.

Constraining Australian and African dust separately with observations offsets some of the difference in the source prescriptions. However, because emission is inferred indirectly by matching observations of other physical quantities (e.g. AOT), the optimal emission need not be identical among the four source prescriptions. This may explain why global emission corresponding to the ZENDER sources remains one and a half times larger than the GINOUX and TEGEN values (Figure 11).

[45] Table 6 shows the value of C normalized by the value from the global optimization (Figure 10). The results show that the most productive source region for a given wind speed (indicated by a higher value of C) is Africa (excluding North America, where total emission is much smaller). In the GINOUX and TEGEN experiments, Africa and Asia emit similar ratios of silt to clay, whereas in the ZENDER experiments, silt emission is largest for Africa. These regional variations of C along with the silt and clay fractions may be spurious, existing only to compensate for errors in AOT and other quantities in our model. Whether these inferred regional variations are valid should be determined by measurement of the emitted size distribution.

5.5. Additional Aerosols

[46] As noted in section 3, the locations for comparison have been selected in order to minimize the presence of other aerosols. Nevertheless, there can be times of the year when the dust load does not constitute the dominant contribution to AOT. To address this contribution by other species we use output from a multi-component aerosol model that calculates the distribution of sulfate, sea salt, black and organic carbon [*Koch*, 2001; *Koch et al.*, 2006; *Koch and Hansen*, 2005].

[47] When the contribution of other aerosols to AOT is included, the optimal distribution corresponds to no clay emission for all source prescriptions (Figure 12). Other aerosols contribute to the overall AOT and obviate the need for clay aerosols. For example, for the GINOUX source, the optimal clay emission is zero, although emission up to 150 Tg/yr is consistent with departures from the minimum error up to 5%. Note that the use of a model to estimate the AOT contribution by other aerosol species introduces an additional uncertainty into the optimization. This uncertainty emphasizes the value of multi-spectral satellite retrievals that distinguish the contribution by dust with greater accuracy.

6. Conclusions

[48] The magnitude of the terrestrial dust cycle remains uncertain, in part because there are few direct observations of soil particles entering the atmosphere. Extrapolation of observed ocean deposition and measurements over specific source regions indicate a range of global emission spanning over two orders of magnitude. Here, we constrain global emission by comparing the dust cycle calculated by the GISS AGCM to many data types including AOT, surface concentration, deposition, and size distribution at a worldwide array of stations. The AGCM dust model is described in a companion article [*Miller et al.*, 2006], which includes a more detailed regional comparison to the observations here.

[49] In order to constrain the dust cycle, we employ a weighted sum of the squared difference between the model and observed values. We minimize this sum to identify the magnitude of the global dust cycle and emission that is in optimal agreement with the observations. This function favors dustier stations close to the source, which is advantageous because model transport and deposition errors increasingly magnify the discrepancy of the model with respect to observations as dust travels downwind. In Appendix A, we show that clay is constrained mainly by AOT and the AERONET size distribution, while surface concentration, deposition, and the size distribution determine the silt contribution (see also Figure 2).

[50] When considered individually, the different data sets point to contrasting optimal values of total emission (Figures 6 and 7). Thus, the magnitude of the dust cycle is very sensitive to the data set used as a constraint, if only one data set is chosen. In contrast, a combination of data sets identifies a consensus optimal solution that generally agrees with all the observations (Table 4), and is much less sensitive to the exclusion of a particular data set (Table 5). For the GINOUX source prescription and the RELEVANT subset of measurements, the global annual emission of particles between 0.1 and 8 μm is 1,534 Tg, comprised of 188 Tg of clay and 1,345 Tg of silt. The total emission is comparable to current model estimates [*Zender et al.*, 2004], although our clay fraction (comprised of particles with radius less than 1μm) is much smaller. Although an increase in the far-traveled silt fraction has been suggested previously by the size distribution measured downwind of African sources, for example, during PRIDE [*Reid et al.*, 2003; *Maring et al.*, 2003], a large silt fraction is indicated by a combination of the data sets we considered, and remains valid even if the size distribution is eliminated. The relatively small model clay fraction consistent with the observations suggests that clay particles are less available for emission than previously assumed by models. An alternative interpretation is that clay is not removed quickly enough in our model as the particles travel away from the source, although this is contradicted by the excessive deposition diagnosed during model transport over the Atlantic [*Miller et al.*, 2006]. We have tried to minimize the effect of deposition errors by defining the error Φ according to (3), which emphasizes measurements near the source.

[51] Uncertainty in our optimal solution results from a number of factors. In Appendix A, we estimate that measurement error and interannual variability, which leads to uncertainty in the observed climatology, contribute less than a few percent to the uncertainty of the optimal global and annual emission. By far the largest contribution to uncertainty results from our prescription of dust source regions. Three additional prescriptions result in optimal emission over 2200 Tg and as high as 2600 Tg. In general, this range indicates that while the environment favorable to dust emission is recognized [*Prospero et al.*, 2002], it remains unsettled how best to specify this environment in a model. Smaller uncertainties of a few hundred Tg result from changing the weighting of individual observations, or excluding a single data set from the evaluation, but these can result in global, annual emission as large as 3000 Tg (Figure 8). This value is substantially larger than emission

estimates from other recent models, but the associated dust cycle remains in good agreement with the observations.

[52] While optimization is intended to constrain model emission, it may inadvertently compensate for model errors. The clay load constrained by AOT will be sensitive to our use of particle optical properties of Saharan dust for all source regions. The optimal dust cycle we identify will be altered by the use of observed winds, as opposed to AGCM values. *Luo et al.* [2003] find that their model's emission is dependent upon their particular choice of reanalysis winds, especially in the Southern Hemisphere. In our model, the error is lowest with the GINOUX representation of preferred sources (for the RELEVANT set of measurements). However, *Zender et al.* [2003] find a different ranking, based upon a different model and transport, albeit with a smaller array of observations. To some extent, the sensitivity to transport and deposition in our model is reduced by the precedence of upwind observations in our error definition (3). Nonetheless, the sensitivity of the optimal dust cycle to its model representation remains an uncertainty that can be quantified only by comparison of the dust cycle calculated by other models to the same observations. Additional uncertainty results from our attempt to match the observations while excluding anthropogenic sources of dust. Whether the contribution of the latter is important remains under debate [*Mahowald et al.*, 2003; *Tegen et al.*, 2004b, 2004a; *Mahowald et al.*, 2004].

[53] Certain source regions such as Australia are only weakly constrained by the observations we considered. There are over two decades of dust storm frequency observations in this region [*Engelstaedter et al.*, 2003], which may reduce the disparity of emission estimates that result from different dust source prescriptions. Our estimate of the optimal dust cycle is also sensitive to the uncertain contribution of other aerosol species to measurements of AOT. The latest generation of satellite retrievals such as MODIS and MISR are able to distinguish dust from other aerosols with greater accuracy. While AOT is a strong constraint upon clay emission, the calculation of the silt load shows the value of continued ground measurements of dust concentration and deposition. Additional observations will result in more confident estimates of the global dust cycle.

Appendix A: Sensitivity of Optimal Emission

[54] In this appendix, we derive a semi-analytic formula for the optimal solution, which allows us to rank the importance of each observation to the optimal solution, as well as assess its uncertainty.

A1. Which Observations Provide the Strongest Constraint?

[55] We make two modifications to our definition of the model error to facilitate a semi-analytic solution. First, we normalize the error Φ with respect to each data set using only the observations, so that S becomes (see equation (4)):

$$S^2 = \frac{1}{M}\sum_{i=1}^{M}\left(X_i^o\right)^2. \tag{A1}$$

Second, we redefine the total error Φ_T, so that its square is a weighted sum of the square of the individual errors Φ (see equation (5)):

$$\Phi_T^2 = \sum_{j=1}^{7} w_j \Phi_j^2 \tag{A2}$$

As a result, the optimal solution is only slightly modified. Total emission is reduced by less than 200 Tg, while the clay component is nearly unchanged.

[56] The optimal solution is derived using trial values of global clay and silt emission computed by the AGCM, denoted by $\mathcal{E}_{c,0}$ and $\mathcal{E}_{s,0}$, respectively. This emission results in contributions by clay and silt particles to model variables such as AOT or surface concentration that can be compared to observations. We define the model contributions by clay and silt in the trial simulation as X_i^c and X_i^s, respectively. (The subscript i refers to a particular observation and varies with location and month of the climatology.) In general, our trial variables will not be in the best possible agreement with the observations. However, because each of these quantities is linear with respect to emission, we can bring the model variables into better agreement by varying the global clay and silt emission, denoted by $\mathcal{E}_c$ and $\mathcal{E}_s$, respectively, with respect to the trial values. Then, the model value X_i^m is:

$$X_i^m \equiv X_i^c \frac{\mathcal{E}_c}{\mathcal{E}_{c,0}} + X_i^s \frac{\mathcal{E}_s}{\mathcal{E}_{s,0}}. \tag{A3}$$

[57] In Figure 10, we locate the minimum total error Φ_T, between the model X_i^m and observations X_i^o by varying the global clay and silt emission through trial and error. Alternatively, we substitute (A3) into (3) and (A2):

$$\Phi_T^2 = \sum_k \frac{w_k}{S_k M_k}\left(X_k^o - X_k^c \frac{\mathcal{E}_c}{\mathcal{E}_{c,0}} - X_k^s \frac{\mathcal{E}_s}{\mathcal{E}_{c,0}}\right)^2. \tag{A4}$$

(Here, the subscript k ranges over all data sets, in addition to all observations within each data set. The quantities w_k, S_k, and M_k depend only upon the data set.) Equation (A4) is a least squares problem [*Press et al.*, 1992, chapter 15], that can be solved for the optimal values of global clay and silt emission, $\mathcal{E}_c$ and $\mathcal{E}_s$, that minimize Φ_T.

[58] To simplify notation, we define non-dimensional values of the observations and model output according to $x_k^o \equiv \sqrt{\frac{w_k}{S_k M_k}}\, X_k^o$, $x_k^c \equiv \sqrt{\frac{w_k}{S_k M_k}}\, X_k^c$, and $x_k^s \equiv \sqrt{\frac{w_k}{S_k M_k}} X_k^s$. Then, setting the differentials of (A4) with respect to $\mathcal{E}_c$ and $\mathcal{E}_s$ equal to zero results in the 'normal equations' [*Press et al.*, 1992, chapter 15]:

$$\begin{aligned} \epsilon_c \sum_k x_k^c x_k^c + \epsilon_s \sum_k x_k^c x_k^s &= \sum_k x_k^c x_k^o \\ \epsilon_c \sum_k x_k^c x_k^s + \epsilon_s \sum_k x_k^s x_k^s &= \sum_k x_k^s x_k^o \end{aligned} \tag{A5}$$

where we have defined $\epsilon_c \equiv \frac{\mathcal{E}_c}{\mathcal{E}_{c,0}}$ and $\varepsilon_s \equiv \frac{\mathcal{E}_s}{\mathcal{E}_{s,0}}$. This has as a solution:

$$\begin{aligned} \epsilon_c &= \frac{1}{\delta_c}\sum_k \left(c_{22} x_k^c - c_{12} x_k^s\right) x_k^o \\ \epsilon_s &= \frac{1}{\delta_c}\sum_k \left(-c_{12} x_k^c + c_{11} x_k^s\right) x_k^o \end{aligned} \tag{A6}$$

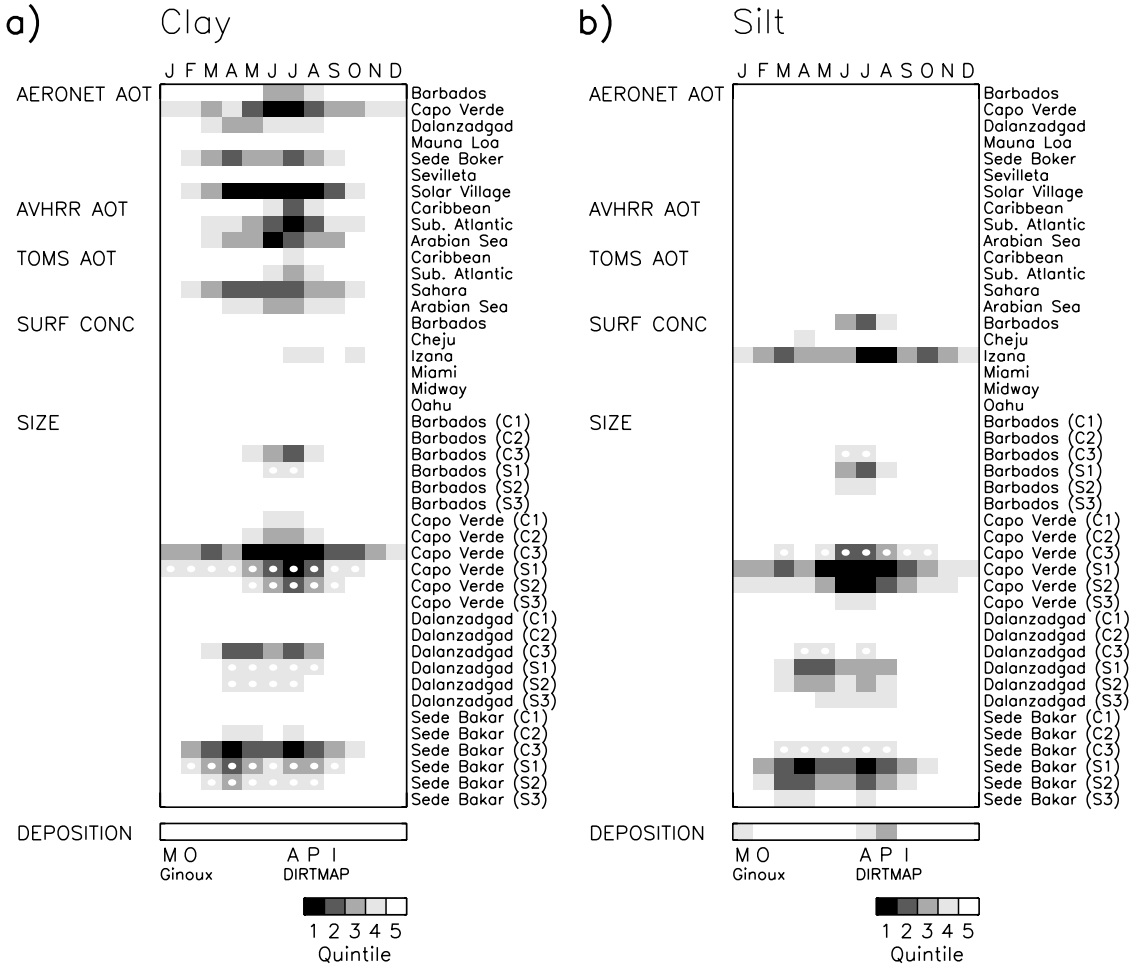

Figure A1. Factors (or 'filters') multiplying the contribution of each observation to the optimal global emission (see equation (A6)). The filters are ranked in magnitude and identified by quintile. The darkest shade indicates filters within the first quintile, while filters within the lowest quintile are indicated by the absence of shading. Negative filters are indicated by a white circle. The observing stations are listed on the vertical axis, while the horizontal axis represents months of the year. The exception is for deposition measurements, whose contribution is shaded on the bottom row. For deposition, 'M' and 'O' represent the Midway and Oahu stations, respectively, while 'A', 'P', and 'I' respectively denote stations within the Atlantic, Pacific, and Indian Ocean. C1, C2, and C3 denote size categories for clay ranging from 0.2–0.3 μm, 0.3–0.6 μm, and 0.6–1 μm. while S1, S2, and S3 denote silt categories ranging from 1–2 μm, 2–4 μm, and 4–8 μm.

where

$$c_{11} = \sum_k x_k^c x_k^c, c_{12} = \sum_k x_k^c x_k^s,$$
$$c_{22} = \sum_k x_k^s x_k^s, \delta_c = c_{11}c_{22} - c_{12}^2. \tag{A7}$$

[59] Equation (A6) shows that each observation x_k^o contributes to ϵ_c and ϵ_s in proportion to $c_{22}\, x_k^c - c_{12}\, x_k^s$ and $-c_{12}\, x_k^c + c_{11} x_k^s$, respectively. These coefficients of proportionality depend only upon the covariance of the model silt and clay values, and are independent of the observations. We refer to them here as 'filters', because they influence the contribution of each observation to the optimal emission. Where the filter is large, the corresponding observation is weighted more heavily in its contribution to the optimal value. The filter corresponding to each observation is shown in Figure A1 for the RELEVANT set of observations and GINOUX source. The filters are ranked and sorted by quintile, with a darker shading representing a higher quintile with larger filter values. Negative products are marked by white circles.

[60] Certain data sets are weighted more heavily, despite our normalization S that makes the contribution to Φ by each data set of potentially the same order (4). For clay emission, filter values are largest for retrievals of AOT and particle size, while surface concentration, size, and to a lesser extent, deposition constrain silt emission with larger weights (Figure A1). In general, observations corresponding to high dust concentration have the largest weights. For example, AOT has a higher filter value at Capo Verde than at a downwind site like Barbados. Similarly, the constraint upon silt emission by surface concentration is more heavily weighted at Izaña than downstream. Observations are also weighted more heavily during months when the concentra-

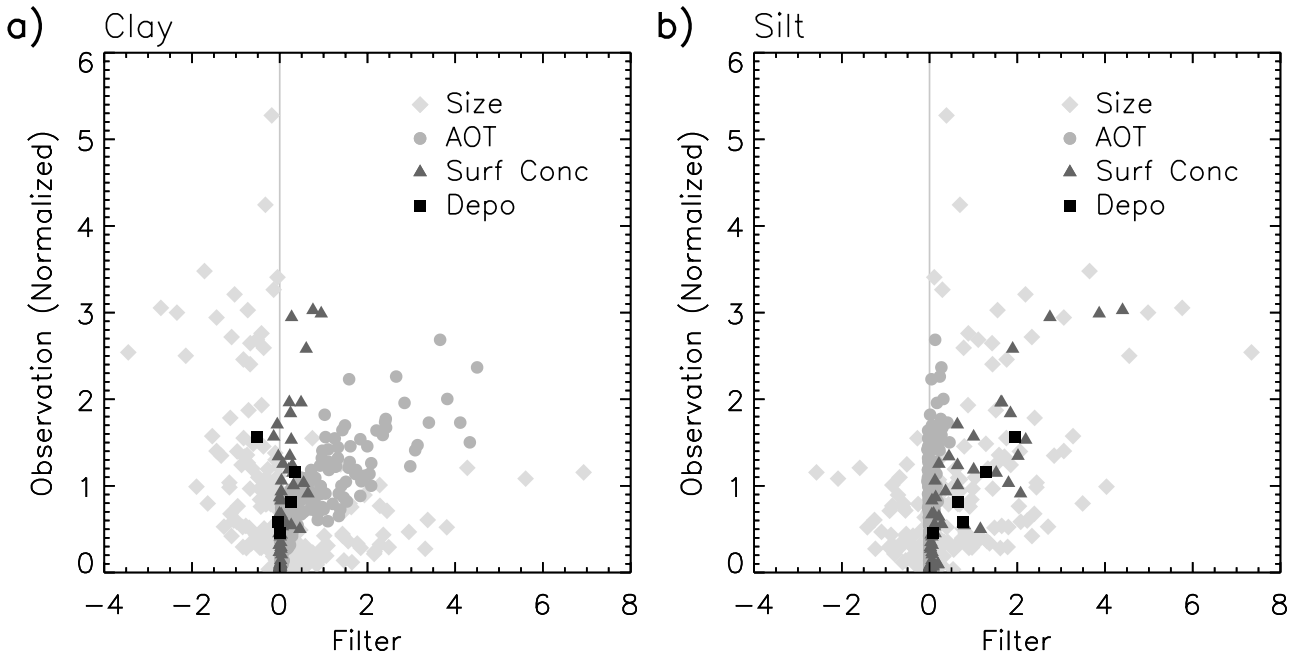

Figure A2. (a) Clay and (b) silt factors (or 'filters') multiplying each observation x_k^o in equation (A6), plotted versus the observation.

tion is high. The filter corresponding to surface concentration at Izaña has a mid-summer maximum, which is associated with the elevation of the model dust plume to the measurement altitude during these months [*Miller et al.*, 2006]. Size retrieval filters are largest in categories where the distribution peaks. Silt retrievals reduce the optimal clay emission by their negative filter values (Figure A1a). Silt is a potential constraint upon clay because of the covariance between the two size categories; variations in silt emission will affect the model's agreement with respect to clay observations.

[61] The strength of the constraint placed upon emission by an observation depends upon the latter's product with its filter. In general, larger filter values (proportional to the model values x_k^c and x_k^s) correspond to larger observed values (Figure A2). For silt particles, the rank correlation between the filter and observations shown in the figure is 0.48, which is highly significant. The correlation is only 0.10 for clay particles, due to the negative filter values associated with the size retrievals, although the correlation rises to 0.56 if absolute values are correlated, and 0.76 if size retrievals are excluded.

[62] The product of an observation x_i^o and its filter, which sums to give the optimal emission according to (A6), is shown in Figure A3. Because of the general correlation between the magnitude of the observed values and the corresponding filter, the product increases approximately as the square of the filter value. This magnifies the effect of the largest observed values upon optimal emission. The strongest constraints upon emission indicated by Figure A3 are generally the most extreme values in Figure A1. This further emphasizes the contribution to the optimal solution of observations in regions of high dust concentration.

[63] It is surprising then, that Pacific stations provide a weaker constraint upon global emission than stations near African and Arabian sources. This is in spite of the proximity of Dalangadzad, which provides both retrievals of AOT and size, to Asian source regions. For silt, the Pacific DIRTMAP observation provides the strongest constraint upon Asian sources. Clay emission is almost entirely constrained in the RELEVANT experiment by observations downwind of Africa and Arabia. Nonetheless, observations that only weakly constrain global emission may be well-simulated by the model. Model agreement with AERONET AOT is better at Dalanzadgad than Solar Village [*Miller et al.*, 2006].

A2. Uncertainty in Global Optimal Emission

[64] Uncertainty in our estimate of the optimal global emission results from measurement error, interannual variability of both the model and observations (which introduces uncertainty in the inferred climatological value), model biases, limited knowledge of the contribution of other aerosol species to the observations, and our arbitrary choice of measurement types and locations. In Section 5, we calculate changes to the optimal global emission that result from using different data sets as a constraint, as well as including other aerosol species in the model comparison. Here, we consider the effect of interannual variability. As shown in *Miller et al.* [2006], this variability is generally within 25% of the observed value. We assume measurement errors are comparatively small, although they are generally not estimated precisely or extensively documented. An estimate of uncertainty requires a number of assumptions that are difficult to verify, so we will not attempt to be precise.

[65] The optimal values of clay and silt emission, $\mathcal{E}_c$ and $\mathcal{E}_s$, are functions of both the observations X_i^o and corresponding model values X_i^m, according to (A6). Imprecise knowledge of the observed and model clima-

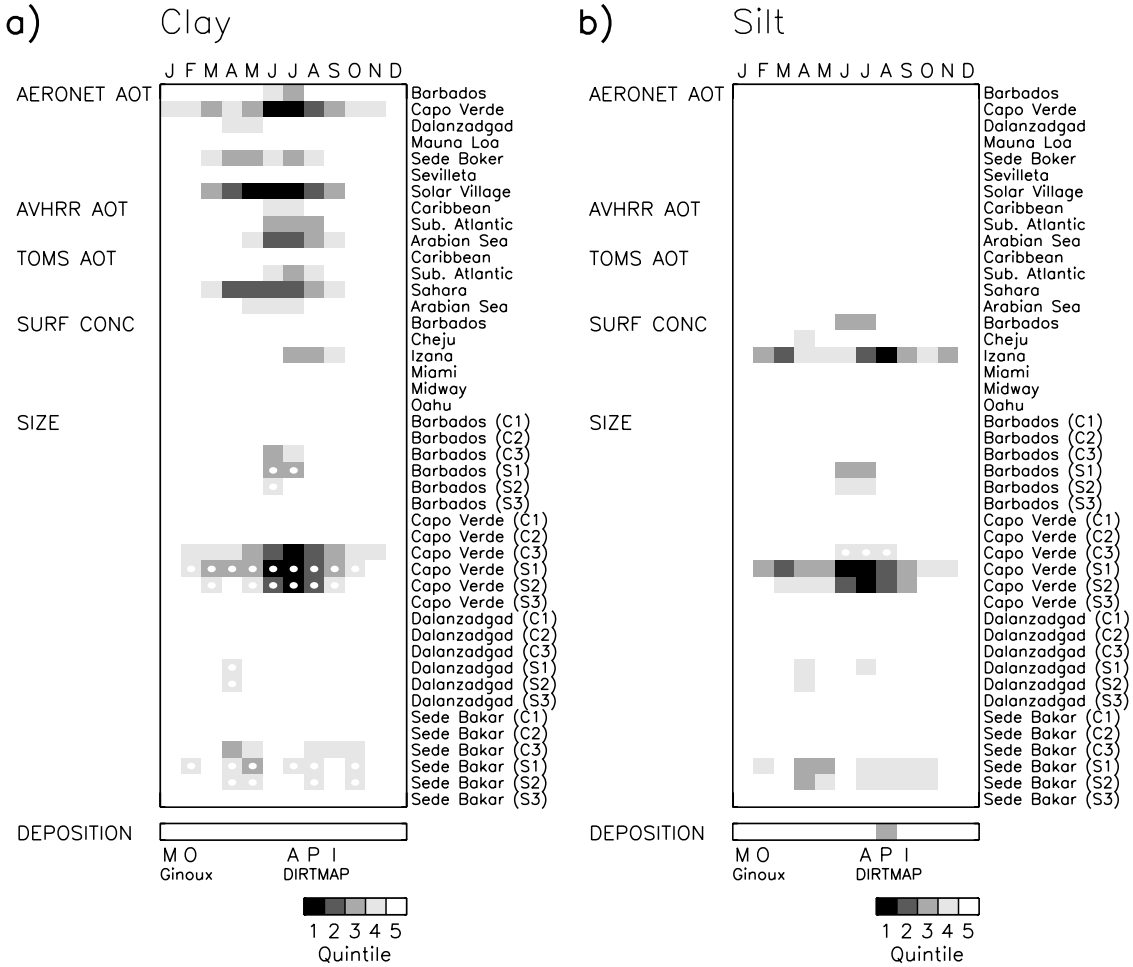

Figure A3. Contribution by quintile of each observation to the optimal values of clay and silt emission. The contribution is defined as the product of each observation x_k^o with its filter; the product is ranked by quintile and plotted as in Figure A1.

tology can be related to an uncertainty in the optimal clay emission:

$$d\,\mathcal{E}_c = \sum_i^N \frac{\partial \mathcal{E}_c}{\partial X_i^o} d\,X_i^o + \sum_i^N \frac{\partial \mathcal{E}_c}{\partial X_i^m} d\,X_i^m, \tag{A8}$$

with a similar equation for silt. The sum is over all N observations, corresponding to different physical quantities, locations, and climatological months.

[66] Assume for simplicity that the model values are known precisely, so that the second sum is zero. (We will relax this assumption below.) To calculate the uncertainty in clay emission, we square the equation and take the expected value (denoted by an overbar):

$$\sigma_c^2 \equiv \overline{(d\,\mathcal{E}_c)^2} = \sum_i^N \sum_j^N \frac{\partial \mathcal{E}_c}{\partial X_i^o} \frac{\partial \mathcal{E}_c}{\partial X_j^o} \overline{d\,X_i^o\; d\,X_j^o}, \tag{A9}$$

where σ_c^2 is the uncertainty of the optimal clay emission. Often, the observation uncertainties are assumed to be independent so that:

$$\overline{d\,X_i^o\; d\,X_j^o} = \delta_{i,j} \overline{(d\,X_i^o)^2}, \tag{A10}$$

where $\delta_{i,j}$ equals unity for i equal to j, and zero otherwise. In this case, the double sum of $N \times N$ values in (A9) reduces to a single sum of N values, yielding the familiar formula for the propagation of errors [*Press et al.*, 1992, chapter 15]:

$$\sigma_c^2 \equiv \overline{(d\,\mathcal{E}_c)^2} = \sum_i^N \left(\frac{\partial \mathcal{E}_c}{\partial X_i^o}\right)^2 \overline{(d\,X_i^o)^2}. \tag{A11}$$

[67] We estimate that the fractional uncertainty of the observations corresponding to interannual variability is of order 25%, so that $d\,X_i^o = 0.25\,X_i^o$ [*Miller et al.*, 2006]. By differentiating the formula for optimal emission (A6) with respect to each observation X_i^o, we calculate that the fractional error of clay and silt emission is of order 0.5% or about 5–10 Tg. The small uncertainty of emission compared to that of the individual observations results from the assumption of independent errors, which largely cancel when considered in aggregate.

[68] In contrast to our assumption of independence, climatologies from nearby measurement locations are likely to have dependent errors as a result of interannual variability. For example, a year with unusually large dust emission from the western Sahara will result in high dust concentration and AOT at most stations downwind over the Atlantic.

To be sure, this correspondence is not precise, and observations at locations along the dust trajectory are increasingly decorrelated with distance.

[69] For the RELEVANT experiment, the observations are grouped into three major downwind regions, corresponding to Saharan, Arabian, and Asian sources. We assume that emission from the three source regions are independent but that all observations downwind of a particular source region are perfectly correlated. In addition, different months of the climatology are assumed to be uncorrelated. Then, the $N = 533$ observations in the RELEVANT case can be divided into 3×12 or 36 groups corresponding to the 3 source regions and 12 months. Each group consists of roughly $\frac{533}{36}$ or 15 observations. The observations within each group are correlated, but are uncorrelated with observations from the other groups. Then, each group contributes 15×15 terms to the double sum, for a total over 36 groups of $15 \times 15 \times 36$ terms. This is to be compared to the 533 terms in (A11), where the double sum is evaluated assuming all the observations are independent. Thus, the uncertainty σ_c derived from (A11) should be increased by the square root of $\frac{15\times15\times36}{533}$ or roughly 4. (An alternative way to visualize this is through the covariance matrix, which is of size $N \times N$ and block diagonal, with each of the 36 blocks of size 15×15. Then, the covariance matrix has roughly $15 \times 15 \times 36$ non-zero terms.)

[70] If we assume that interannual variability in the model is comparable to the observed value, then the uncertainty increases by another factor of roughly $\sqrt{2}$, so that the fractional uncertainty according to (A9) is around $4 \times \sqrt{2}$ times 0.5%. That is, σ_c, the uncertainty in clay emission due to interannual variability, is probably under 4%. However, we emphasize that our estimate of σ_c is intended as an upper bound. In practice, each group of roughly 15 observations contributing to the double sum in (A9) will be dominated by a few observations where the dust concentration is highest.

[71] In summary, we suggest that interannual variability results in uncertainty of the estimated emission that is probably smaller than a few percent. This uncertainty is augmented by model biases (due to the source prescription, for example) and our subjective choice of data types and locations.

Appendix B: Dependence of Inferred Emission Upon Observation Distance From Source

[72] Using a heuristic example, we illustrate how distance of an observing station from the source affects the magnitude of the dust cycle inferred from observations.

[73] Say that the observed dust load L_o varies with distance x downstream from the source according to:

$$L_o(x) = L_{o,0} \exp\left(\frac{-x}{\Delta}\right), \tag{B1}$$

and that our model predicts the load $L_m(x)$ according to:

$$L_m(x) = L_{m,0} \exp\left(\frac{-x}{\delta}\right), \tag{B2}$$

where because of excessive wet deposition (or weaker transport), the modeled dust load decreases more abruptly downstream than observed: i.e. $\delta < \Delta$.

[74] If we constrain $L_{m,0}$ using the observed value at the point x_0, then:

$$L_{m,0} \exp\left(\frac{-x_0}{\delta}\right) = L_{o,0} \exp\left(\frac{-x_0}{\Delta}\right), \tag{B3}$$

so that:

$$L_{m,0} = L_{o,0} \exp\left(\frac{x_0(\Delta - \delta)}{\Delta\delta}\right) > L_{o,0}. \tag{B4}$$

The overestimate of $L_{m,0}$ increases exponentially with the distance of the observing site downstream. Were the model decay scale too large (say due to insufficient deposition), then $L_{m,0} < L_{o,0}$, and the underestimate would again increase with distance of the observing site from the source. In general, constraining the model with observations leads to the smallest error for observing sites that are nearest the source. This is a consequence of any unrealistic behavior in the model (including errors in deposition or transport) as dust moves away from the source, and is separate from the effect of any error in the observations themselves.

[75] **Acknowledgments.** This article was improved by the suggestions of Natalie Mahowald and an anonymous reviewer. We are grateful to Michael Mishchenko, and Catherine Prigent for their comments. We also thank Chuck McClain, Brent Holben, Didier Tanré, Ross Mitchell, Mary Jane Bartholomew, Jeannette Vandenbosch, and John Vande Castle for the AERONET data sets. We are grateful to Omar Torres for the TOMS AOT and to Joseph Prospero and Dennis Savoie for the surface concentration measurements. Our thanks also go to Catherine Prigent for the ERS data set. This work was supported by the Climate Dynamics Program of the National Science Foundation through ATM-01-24258. Reha V. Cakmur received additional support as a Research Associate of the National Academy of Sciences with funding provided by Tsengdar Lee and Don Anderson of the NASA Atmospheric Modeling Program.

References

Alfaro, S. C., and L. Gomes (2001), Modeling mineral aerosol production by wind erosion: Emission intensities and aerosol size distributions in source areas., *J. Geophys. Res.*, *106*, 18,075–18,084.

Bory, A., et al. (2001), Downward particle fluxes within different productivity regimes off the Mauritanian upwelling zone (EUMELI program), *Deep Sea Res. I*, *48*, 2251–2282.

Bretherton, C. S., and D. S. Battisti (2000), An interpretation of the results from atmospheric general circulation models forced by the time history of the observed sea surface temperature distribution, *Geophys. Res. Lett.*, *27*(6), 767–770.

Cakmur, R. V., R. L. Miller, and O. Torres (2004), Incorporating the effect of small-scale circulations upon dust emission in atmospheric general circulation model, *J. Geophys. Res.*, *109*, D07201, doi:10.1029/2003JD004067.

Cheng, Y., V. M. Canuto, and A. M. Howard (2002), An improved turbulence model for the turbulent PBL, *J. Atmos. Sci.*, *59*, 1550–1565.

Chiapello, I., G. Bergametti, L. Gomes, B. Chatenet, F. Dulac, J. Pimenta, and E. Santos Suarez (1995), An additional low layer transport of Sahelian and Saharan dust over the north-eastern tropical Atlantic, *Geophys. Res. Lett.*, *22*, 3191–3194.

Chiapello, I., P. Goloub, G. Tanre, A. Marchand, J. Herman, and O. Torres (2000), Aerosol detection by TOMS and POLDER over oceanic regions, *J. Geophys. Res.*, *105*, 7133–7142.

Chin, M., D. J. Jacob, M. Gardner, M. S. Foreman-Fowler, and P. A. Spiro (1996), A global three-dimensional model of tropospheric sulfate, *J. Geophys. Res.*, *101*, 18,667–18,690.

Chu, D. A., Y. J. Kaufman, C. Ichoku, L. A. Remer, D. Tanré, and B. N. Holben (2002), Validation of MODIS aerosol optical depth retrieval over land, *Geophys. Res. Lett.*, *29*(12), 8007, doi:10.1029/2001GL013205.

Dubovik, O., and M. King (2000), A flexible inversion algorithm for retrieval of aerosol optical properties from Sun and sky radiance measurements, *J. Geophys. Res.*, *105*, 20,673–20,696.

Dubovik, O., A. Smirnov, B. Holben, M. King, Y. Kaufman, T. Eck, and I. Slutsker (2000), Accuracy assessment of aerosol optical properties

retrieved from Aerosol Robotic Network (AERONET) Sun and sky radiance measurements, *J. Geophys. Res.*, *105*, 9791–9806.
Dubovik, O., B. N. Holben, T. F. Eck, A. Smirnov, Y. J. Kaufman, M. D. King, D. Tanré, and I. Slutsker (2002), Variability of absorption and optical properties of key aerosol types observed in worldwide locations, *J. Atmos. Sci.*, *59*, 590–608.
Duce, R. (1995), Sources, distributions, and fluxes of mineral aerosols and their relationship to climate change, in *Dahlem Workshop on Aerosol Forcing of Climate*, *Environmental Sciences Research Report 17*, edited by R. J. Charlson and J. Heintzenber, pp. 43–72, John Wiley, Hoboken, N. J.
Dufresne, J. L., C. Gautier, P. Ricchiazzi, and Y. Fouquart (2002), Longwave scattering effects of mineral aerosols, *J. Atmos. Sci.*, *59*, 1959–1966.
Engelstaedter, S., K. E. Kohfeld, I. Tegen, and S. P. Harrison (2003), Controls of dust emissions by vegetation and topographic depressions: An evaluation using dust storm frequency data, *Geophys. Res. Lett.*, *30*(6), 1294, doi:10.1029/2002GL016471.
Geogdzhayev, I. V., M. I. Mishchenko, W. B. Rossow, B. Cairns, and A. A. Lacis (2002), Global two-channel AVHRR retrievals of aerosol properties over the ocean for the period of NOAA-9 observations and preliminary retrievals using NOAA-7 and NOAA-11 data, *J. Atmos. Sci.*, *59*, 262–278.
Gillette, D. (1974), On the production of soil wind erosion aerosols having the potential for long range transport, *J. Rech. Atmos.*, *8*, 735–744.
Gillette, D. (1978), A wind tunnel simulation of the erosion of soil: Effect of soil texture, sandblasting, wind speed, and soil consolidation on dust production, *Atmos. Environ.*, *12*, 1735–1743.
Ginoux, P., M. Chin, I. Tegen, J. Prospero, B. Holben, O. Dubovik, and S. J. Lin (2001), Sources and distributions of aerosols simulated with the GOCART model, *J. Geophys. Res.*, *106*, 20,255–20,273.
Goudie, A. S. (1983), Dust storms in space and time, *Prog. Phys. Geogr.*, *7*, 502–530.
Goudie, A. S., and N. J. Middleton (2001), Saharan dust storms: Nature and consequences, *Earth Sci. Rev.*, *56*, 179–204.
Grini, A., C. S. Zender, and P. R. Colarco (2002), Saltation sandblasting behavior during mineral aerosol production, *Geophys. Res. Lett.*, *29*(18), 1868, doi:10.1029/2002GL015248.
Grini, A., G. Myhre, C. S. Zender, and I. S. A. Isaksen (2005), Model simulations of dust sources and transport in the global atmosphere: Effects of soil erodibility and wind speed variability, *J. Geophys. Res.*, *110*, D02205, doi:10.1029/2004JD005037.
Holben, B., et al. (1998), Aeronet—A federated instrument network and data archive for aerosol characterization, *Remote Sens. Environ.*, *66*, 1–16.
Holben, B. N., et al. (2001), An emerging ground-based climatology: Aerosol optical depth from AERONET, *J. Geophys. Res.*, *106*, 12,067–12,097.
Houghton, J. T., Y. Ding, D. J. Griggs, M. Noguer, P. J. van der Linden, X. Dai, K. Maskell, and C. A. Johnson (Eds.) (2001), *Climate Change 2001: The Scientific Basis. Contribution of Working Group I to the Third Assessment Report of the Intergovernmental Panel on Climate Change*, Cambridge Univ. Press, New York.
Iversen, J., and B. White (1982), Saltation threshold on Earth, Mars and Venus, *Sedimentology*, *29*, 111–119.
Kahn, R., P. Banerjee, and D. McDonald (2001), The sensitivity of multiangle imaging to natural mixtures of aerosols over ocean, *J. Geophys. Res.*, *106*, 18,219–18,238.
Koch, D. (2001), Transport and direct radiative forcing of carbonaceous and sulfate aerosols in the GISS GCM, *J. Geophys. Res.*, *106*, 20,311–20,332.
Koch, D., and J. Hansen (2005), Distant origins of Arctic black carbon: A GISS ModelE experiment, *J. Geophys. Res.*, *110*, D04204, doi:10.1029/2004JD005296.
Koch, D., D. Jacob, I. Tegen, D. Rind, and M. Chin (1999), Tropospheric sulfur simulation and sulfate direct radiative forcing in the Goddard Institute for Space Studies general circulation model, *J. Geophys. Res.*, *104*, 23,799–23,822.
Koch, D., G. Schmidt, and C. Field (2006), Sulfur, sea salt, and radionuclide aerosols in GISS modelE, *J. Geophys. Res.*, doi:10.1029/2004JD005550, in press.
Kohfeld, K. E., and S. P. Harrison (2001), DIRTMAP: The geological record of dust, *Earth Sci. Rev.*, *54*, 81–114.
Liu, L., M. I. Mishchenko, I. Geogdzhayev, A. Smirnov, S. M. Sakerin, D. M. Kabanov, and O. A. Ershov (2004), Global validation of two-channel AVHRR aerosol optical thickness retrievals over the oceans, *J. Quant. Spectrosc. Radiat. Transfer*, *88*, 97–109.
Luo, C., N. M. Mahowald, and J. Corral (2003), Sensitivity study of meteorological parameters on mineral aerosol mobilization, transport, and distribution, *J. Geophys. Res.*, *108*(D15), 4447, doi:10.1029/2003JD003483.
Mahowald, N. M., C. S. Zender, C. Luo, D. Savoie, O. Torres, and J. del Corral (2002), Understanding the 30-year Barbados desert dust record, *J. Geophys. Res.*, *107*(D21), 4561, doi:10.1029/2002JD002097.
Mahowald, N. M., R. G. Bryant, J. Corral, and L. Steinberger (2003), Ephemeral lakes and desert dust sources, *Geophys. Res. Lett.*, *30*(2), 1074, doi:10.1029/2002GL016041.
Mahowald, N. M., G. D. R. Rivera, and C. Luo (2004), Comment on "Relative importance of climate and land use in determining present and future global soil dust emission" by I. Tegen et al., *Geophys. Res. Lett.*, *31*, L24105, doi:10.1029/2004GL021272.
Maring, H., D. L. Savoie, M. A. Izaguirre, L. Custals, and J. S. Reid (2003), Mineral dust aerosol size distribution change during atmospheric transport, *J. Geophys. Res.*, *108*(D19), 8592, doi:10.1029/2002JD002536.
Marticorena, B., and G. Bergametti (1996), Two-year simulations of seasonal and interannual changes of the Saharan dust emissions, *Geophys. Res. Lett.*, *23*, 1921–1924.
Marticorena, B., G. Bergametti, and M. Legrand (1999), Comparison of emission models used for large scale simulation of the mineral dust cycle, *Contrib. Atmos. Phys.*, *72*, 151–160.
Miller, R.L., I. Tegen, and J. Perlwitz (2004), Surface radiative forcing by soil dust aerosols and the hydrologic cycle, *J. Geophys. Res.*, *109*, D04203, doi:10.1029/2003JD004085.
Miller, R. L., et al. (2006), Mineral dust aerosols in the NASA Goddard Institute for Space Sciences ModelE Atmospheric General Circulation Model, *J. Geophys. Res.*, *111*, D06208, doi:10.1029/2005JD005796.
Mishchenko, M., A. Lacis, B. Carlson, and L. Travis (1995), Nonsphericitiy of dust-like tropospheric aerosols: Implications for aerosol remote sensing and climate, *Geophys. Res. Lett.*, *22*, 1077–1080.
Mishchenko, M. I., I. V. Geogdzhayev, B. Cairns, W. B. Rossow, and A. A. Lacis (1999), Aerosol retrievals over the ocean by use of channels 1 and 2 AVHRR data: Sensitivity analysis and preliminary results, *Appl. Opt.*, *38*, 7325–7341.
Mishchenko, M. I., I. V. Geogdzhayev, L. Liu, J. A. Ogren, A. A. Lacis, W. B. Rossow, J. W. Hovenier, H. Volten, and O. Muoz (2003), Aerosol retrievals from AVHRR radiances: Effects of particle nonsphericity and absorption and an updated long-term global climatology of aerosol properties, *J. Quant. Spectrosc. Radiat. Transfer*, *79/80*, 953–972.
Myhre, G., et al. (2004), Intercomparison of satellite retrieved aerosol optical depth over the ocean, *J. Atmos. Sci.*, *61*, 499–513.
Penner, J. E., et al. (2001), Aerosols, their direct and indirect effects, in *Climate Change 2001: The Scientific Basis. Contribution of Working Group I to the Third Assessment Report of the Intergovernmental Panel on Climate Change*, edited by J. Houghton et al., pp. 289–348, Cambridge Univ. Press, New York.
Prather, M. J. (1986), Numerical advection by conservation of second-order moments, *J. Geophys. Res.*, *91*, 6671–6681.
Press, W. H., S. A. Teukolsky, W. T. Vetterling, and B. P. Flannery (1992), *Numerical Recipes in Fortran 77: The Art of Scientific Computing*, 2nd ed., Cambridge Univ. Press, New York.
Prigent, C., F. Aires, W. Rossow, and E. Matthews (2001), Joint characterization of vegetation by satellite observations from visible to microwave wavelengths: A sensitivity analysis, *J. Geophys. Res.*, *106*, 20,665–20,685.
Prigent, C., I. Tegen, P. Aires, B. Marticorena, and M. Zribi (2005), Estimation of the aerodynamic roughness length in arid and semi-arid regions over the globe with the ERS scatterometer, *J. Geophys. Res.*, *110*, D09205, doi:10.1029/2004JD005370.
Prospero, J. (1996), The atmospheric transport of particles to the ocean, in *Particle Flux in the Ocean*, edited by V. Ittekkot, P. Schäfer, S. Honjo, and P. J. Depetris, chap. 3, pp. 19–56, John Wiley, Hoboken, N. J.
Prospero, J. M., P. Ginoux, O. Torres, S. E. Nicholson, and T. E. Gill (2002), Environmental characterization of global sources of atmospheric soil dust identified with the Nimbus 7 total ozone mapping spectrometer (TOMS) absorbing aerosol product, *Rev. Geophys.*, *40*(1), 1002, doi:10.1029/2000RG000095.
Reid, J. S., et al. (2003), Comparison of size and morphological measurements of coarse mode dust particles from Africa, *J. Geophys. Res.*, *108*(D19), 8593, doi:10.1029/2002JD002485.
Remer, L. A., et al. (2002), Validation of MODIS aerosol retrieval over ocean, *Geophys. Res. Lett.*, *29*(12), 8008, doi:10.1029/2001GL013204.
Savoie, D., and J. Prospero (1977), Aerosol concentration statistics for the northern tropical Atlantic, *J. Geophys. Res.*, *82*, 5954–5964.
Schmidt, G. A., et al. (2006), Present day atmospheric simulations using GISS modelE: Comparison to in-situ, satellite and reanalysis data, *J. Clim.*, *19*, 153–192.
Schutz, L. (1980), Long range transport of desert dust with special emphasis on the Sahara, *Ann. N. Y. Acad. Sci.*, *338*, 515–532.

Shao, Y., M. Raupach, and P. Findlater (1993), Effect of saltation bombardment on the entrainment of dust by wind, *J. Geophys. Res.*, *98*, 12,719–12,726.

Shao, Y., M. R. Raupach, and J. F. Leys (1996), A model for predicting aeolian sand drift and dust entrainment on scales from paddock to region, *Aust. J. Soil Res.*, *34*, 309–342.

Sinyuk, A., O. Torres, and O. Dubovik (2003), Combined use of satellite and surface observations to infer the imaginary part of refractive index of Saharan dust, *Geophys. Res. Lett.*, *30*(2), 1081, doi:10.1029/2002GL016189.

Swap, R., S. Ulanski, M. Cobbett, and M. Garstang (1996), Temporal and spatial characteristics of Saharan dust outbreaks, *J. Geophys. Res.*, *101*, 4205–4220.

Tegen, I., and I. Fung (1994), Modeling of mineral dust in the atmosphere: Sources, transport, and optical thickness, *J. Geophys. Res.*, *99*, 22,897–22,914.

Tegen, I., and A. A. Lacis (1996), Modeling of particle influence on the radiative properties of mineral dust aerosol, *J. Geophys. Res.*, *101*, 19,237–19,244.

Tegen, I., and R. L. Miller (1998), A general circulation model study on the interannual variability of soil dust aerosol, *J. Geophys. Res.*, *103*, 25,975–25,995.

Tegen, I., P. Hollrig, M. Chin, I. Fung, D. Jacob, and J. Penner (1997), Contribution of different aerosol species to the global aerosol extinction optical thickness: Estimates from model results, *J. Geophys. Res.*, *102*, 23,895–23,915.

Tegen, I., S. P. Harrison, K. Kohfeld, I. C. Prentice, M. Coe, and M. Heimann (2002), Impact of vegetation and preferential source areas on global dust aerosol: Results from a model study, *J. Geophys. Res.*, *107*(D21), 4576, doi:10.1029/2001JD000963.

Tegen, I., M. Werner, S. P. Harrison, and K. E. Kohfeld (2004a), Reply to comment by N. M. Mahowald et al. on "Relative importance of climate and land use in determining present and future global soil dust emission," *Geophys. Res. Lett.*, *31*, L24106, doi:10.1029/2004GL021560.

Tegen, I., M. Werner, S. P. Harrison, and K. E. Kohfeld (2004b), Relative importance of climate and land use in determining present and future global soil dust emission, *Geophys. Res. Lett.*, *31*, L05105, doi:10.1029/2003GL019216.

Torres, O., P. K. Bhartia, J. R. Herman, A. Sinyuk, P. Ginoux, and B. Holben (2002), A long-term record of aerosol optical depth from TOMS observations and comparison to AERONET measurements, *J. Atmos. Sci.*, *59*, 398–413.

Uematsu, M., R. A. Duce, and J. M. Prospero (1985), Deposition of atmospheric mineral particles in the North Pacific Ocean, *J. Atmos. Chem.*, *3*, 123–138.

Yu, E. F., R. Francois, M. P. Bacon, and A. P. Fleer (2001), Fluxes of 230th and 231pa to the deep sea: Implications for the interpretation of excess 230th and 231pa/230th profiles in sediments, *Earth Planet. Sci. Lett.*, *19*, 1219–1230.

Zender, C. S., D. Newman, and O. Torres (2003), Spatial heterogeneity in aeolian erodibility: Uniform, topographic, geomorphologic, and hydrologic hypotheses, *J. Geophys. Res.*, *108*(D17), 4543, doi:10.1029/2002JD003039.

Zender, C. S., R. L. Miller, and I. Tegen (2004), Quantifying mineral dust mass budgets: Systematic terminology, constraints, and current estimates, *Eos Trans. AGU*, *85*.

Zhang, X. Y., R. Arimoto, and Z. S. An (1997), Dust emission from Chinese desert sources linked to variations in atmospheric circulation, *J. Geophys. Res.*, *102*, 28,041–28,047.

Zobler, L. (1986), A world soil file for global climate modeling, *NASA Tech. Rep.*, *TM-87802*.

R. V. Cakmur, I. V. Geogdzhayev, and D. Koch, NASA Goddard Institute for Space Studies, 2880 Broadway, New York, NY 10025, USA. (rcakmur@giss.nasa.gov; igeogdzhayev@giss.nasa.gov; dkoch@giss.nasa.gov)

P. Ginoux, Geophysical Fluid Dynamics Laboratory, NOAA, Princeton Forrestal Campus Route 1, P.O. Box 308, Princeton, NJ 08542-0308, USA. (paul.ginoux@noaa.gov)

K. E. Kohfeld, School of Earth and Environmental Sciences, Queens College, City University of New York, 65-30 Kissena Blvd., Flushing, NY 11367, USA. (kek@qc.edu)

R. L. Miller and J. Perlwitz, Department of Applied Physics and Applied Math, Columbia University, 2880 Broadway, New York, NY 10025, USA. (rlm15@columbia.edu; jp544@columbia.edu)

I. Tegen, Leibniz Institute for Tropospheric Research, Permoserstr. 15, 04318 Leipzig, Germany. (itegen@tropos.de)

C. S. Zender, Department of Earth System Science, University of California, Irvine, 205 Physical Sciences Research Facility, Irvine, CA 92697-3100, USA. (zender@uci.edu)